Methodological Aspects of Lymphatic Mapping: Radiopharmaceuticals, Multimodal Lymphatic Mapping Agents, Instrumentations

3

Francesco Bartoli, Giuseppina Bisogni, Sara Vitali,
Angela G. Cataldi, Alberto Del Guerra, Giuliano Mariani,
and Paola A. Erba

Contents

Learning Objectives
- To describe the radiopharmaceuticals; iodine-based CT contrast agents; contrast agents for MR, MRL, and PET/MRI; contrast-enhanced ultrasound imaging; optical imaging agents; and multimodal tracers
- To understand the basic concepts behind the radiopharmaceuticals and instrumentations used for lymphoscintigraphy and radioguided surgery
- To outline the most recent advances in radiopharmaceuticals and instrumentations
- To explain the working principles of handheld gamma probes and their most significant parameters, including sensitivity, spatial resolution, energy resolution, and signal-to-noise ratio
- To review the available handheld gamma probes and portable imaging devices and their clinical implementation
- To describe the basic concepts and the equipment for the use of indocyanine green fluorescence technique in surgery

F. Bartoli · S. Vitali · A. G. Cataldi · G. Mariani · P. A. Erba (✉)
Regional Center of Nuclear Medicine, Department of Translational Research and Advanced Technologies in Medicine and Surgery, University of Pisa, Pisa, Italy
e-mail: paola.erba@unipi.it

G. Bisogni · A. Del Guerra
"Enrico Fermi" Department of Physics, University of Pisa, Pisa, Italy

3.1 Introduction

Exploration of lymphatic circulation with radiopharmaceuticals constitutes one of the earliest applications of nuclear medicine, dating back to the early 1950s and steadily growing throughout the 1960s. A potent impetus to further growth

in the clinical applications of lymphoscintigraphy derived from the introduction of agents for lymphatic mapping labeled with technetium-99m (^{99m}Tc). Up until the early 1990s, the predominant applications of lymphoscintigraphy were for assessing lymphatic circulation in patients with peripheral edema (to discriminate edema caused by insufficiency of venous drainage from edema caused by insufficiency of lymphatic drainage) and for assessing the lymph node tumor status in patients with cancer (based on absent lymph node visualization along a certain lymphatic basin in case of massive lymph node metastasis).

Starting in 1992–1993, a real revolution occurred with the use of lymphoscintigraphy for sentinel lymph node (SLN) mapping, initially in patients with cutaneous melanoma or with breast cancer, but soon expanding to include a variety of other solid epithelial cancers. SLN mapping combined with radioguided sentinel lymph node biopsy (SLNB) currently constitutes _the_ standard of care for patients with melanoma, breast cancer, penile cancer, head and neck squamous cell cancers, and gynecological malignancies (primarily vulvar cancer and cervical cancer), while numerous clinical trials for validation of this approach are under way in patients with prostate cancer and, among others, cancers of the gastrointestinal tract. Thus, SLN mapping is by far the most common application worldwide of lymphoscintigraphy. On the other hand, peripheral lymphoscintigraphy in patients with edema or with intracavitary effusions maintains a well-established role in the clinical workup of these conditions—whereas the original use of lymphoscintigraphy per se for assessing the tumor status of lymph nodes in patients with cancers has completely vanished.

Advances in the design of novel radiopharmaceuticals for lymphatic mapping have gone in parallel with technological advances in instrumentations, both for external imaging and for intraoperative use during radioguided surgery. Technological advances also favor the development of hybrid imaging agents with multiple signatures (radioactive, optical, X-ray, or MR contrast) to take maximum advantage from the synergistic combination of different agents with different biological and physical properties—to the final best clinical benefit to patients.

This chapter reviews the status of the art of lymphatic mapping with regard to both the imaging agents employed and the instrumentations used for these investigations.

3.2 Radiopharmaceuticals for Lymphatic Mapping

3.2.1 Radiocolloids and Other Agents for SLN Mapping

Deposition of radioactive colloids in regional lymph nodes (LNs) was first observed by Walker after subcutaneous injection of colloidal gold (^{198}Au) [1]. Since a significant fraction of the activity remained at the injection site after subcutaneous administration of colloidal ^{198}Au (a radionuclide with a significant component of beta decay), radiation burden at the injection site limited the activity that could be safely administered. This led to search for agents with more favorable physical characteristics.

^{198}Au was soon replaced with particulate materials labeled with the most widely employed radionuclide for routine diagnostic procedures, i.e., ^{99m}Tc ($T_{1/2} = 6$ h, exclusive 140 keV gamma radiation, available locally through a generator). The agents developed to this purpose include, among others, ^{99m}Tc-sulfur colloids, ^{99m}Tc-rhenium sulfide, ^{99m}Tc-nano- and micro-aggregated albumin, and ^{99m}Tc-antimony sulfide [2–14]. Neither ^{99m}Tc-antimony sulfide nor ^{99m}Tc-human serum albumin is currently commercially available in the United States. ^{99m}Tc-albumin nanocolloid (Nanocoll®) and ^{99m}Tc-rhenium sulfide colloids are used in Europe [15–18]. Filtered ^{99m}Tc-sulfur colloid (to limit particle size to about <200 nm or about <100 nm—depending on the pore size of the Millipore filter used) is one of the most commonly employed radiopharmaceuticals for lymphoscintigraphy in the United States. In addition, other radiocolloids such as ^{99m}Tc-stannous phytate [3], denatured ^{99m}Tc-collagen colloid, and ^{99m}Tc-stannous fluoride can be used. ^{99m}Tc-labeled Dextran 70, a sucrose polymer of high molecule weight, is another radiopharmaceutical option that can be used for SLN detection [19]; although it is not a true colloid, this compound behaves in a similar fashion as radiocolloids following interstitial injection. Table 3.1 lists the main features of radiopharmaceuticals that have been employed for lymphoscintigraphy, while Figs. 3.1 and 3.2 show the considerable variability in particle size among different preparations.

Generally, the labeling procedure consists of the adsorption of ^{99m}Tc on the particle's surface at nonspecific sites. Colloid quantity, and hence the available adsorption surface,

Table 3.1 Colloidal radiotracers and their particle size (modified from Bergqvist et al. [5])

Radiocolloid	Particle size	References
^{198}Au-colloid	5 nm; 9–15 nm	[4, 20]
^{99m}Tc-rhenium colloid (TCK-1)	10–40 nm; 50–500 nm	[14, 21]
^{99m}Tc-rhenium colloid (TCK-17)	50–200 nm; 45 nm; 3–15 nm	[14, 22]
^{99m}Tc-antimony sulfur colloid	2–15 nm; 40 nm	[14, 23]
^{99m}Tc-sulfur colloid (unfiltered)	100–1000 nm	[24]
^{99m}Tc-sulfur colloid (filtered)	38 nm (mean)	[25]
^{99m}Tc-stannous sulfur colloid	20–60 nm	[26]
^{99m}Tc-albumin nanocolloid (Nanocoll)	<80 nm	[27]
^{99m}Tc-microaggregated albumin (Microlite)	10 nm	[14]

must be used in large excess. In other cases, the labeling procedure is carried out as a coprecipitation process of ^{99m}Tc (Fig. 3.3).

Many factors influence transport of molecules from the interstitium to the lymphatic vessels. Since solutes must interact and cross over with components of the extracellular matrix to enter the lymphatic circulation, extracellular matrix composition and solute properties have significant influence on their ability to move through the interstitium into the lymphatics [28]. The most important properties of molecules in this regard are weight, size, shape, and charge [29–31].

Although molecules are transported both by convection and by diffusion, their size has a major impact on which mechanism predominates [32, 33]. Small molecules are primarily transported by diffusion, which is a slow process over longer distances. The slower transport of the largest molecules is explained by mechanical interaction with the extracellular matrix components, a mechanism that slows down movements of the molecules.
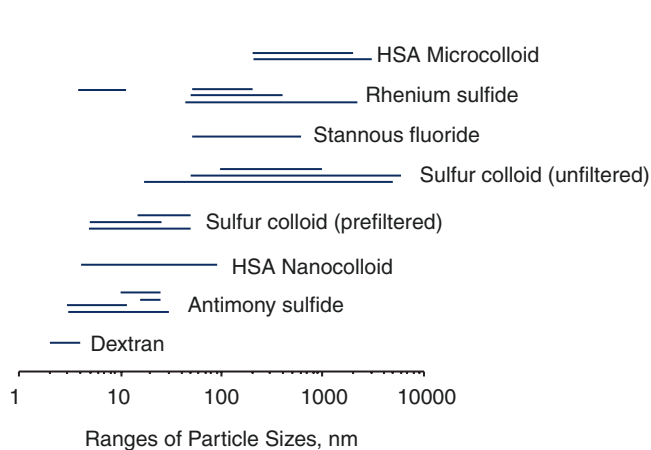
Uptake and retention of radiocolloids in lymph nodes greatly depend on the fact that they undergo phagocytosis once they have entered into the lymphatic circulation and are transported to the lymph nodes. The lymph node is a highly complex structure that contains lymphocytes, plasma cells, and macrophages in a collagen sheath. One fraction of the colloid remains inside the lymph node, where phagocytosis by macrophages occurs. The remaining portion, especially the smaller size fraction, proceeds through the efferent lymph vessels toward the next lymph node(s).

Colloids enter and exit the lymphatic circulation with different speeds depending on their sizes. Their migration through the lymphatic system is also inversely related to particle size. Particles smaller than a few nanometers usually leak into blood capillaries, whereas larger particles (up to about 100 nm) can enter the lymphatic capillaries and be transported to lymph nodes, where phagocytosis takes place [34]. Very small particles (<30 nm) migrate rapidly, with a
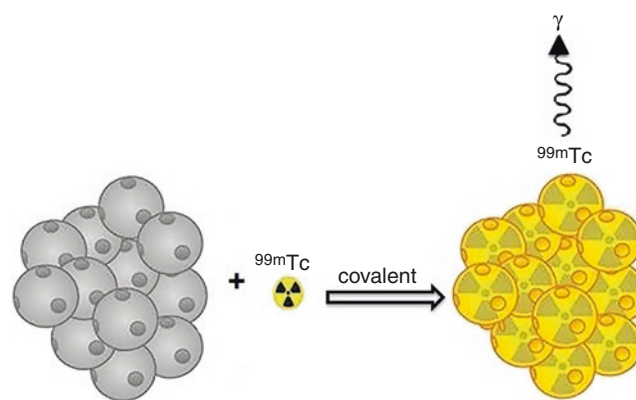
Fig. 3.1 Schematic representation of the ranges of particle sizes in nm in the main radiopharmaceuticals employed for lymphoscintigraphy. *HSA* human serum albumin

Fig. 3.3 Radiolabeling of nanocolloids with ^{99m}Tc (*reproduced with permission from Buckle T, van Leeuwen AC, Chin PT, Janssen H, Muller SH, Jonkers J, et al. A self-assembled multimodal complex for combined pre- and intraoperative imaging of the SLN. Nanotechnology. 2010;21(35):355101*)
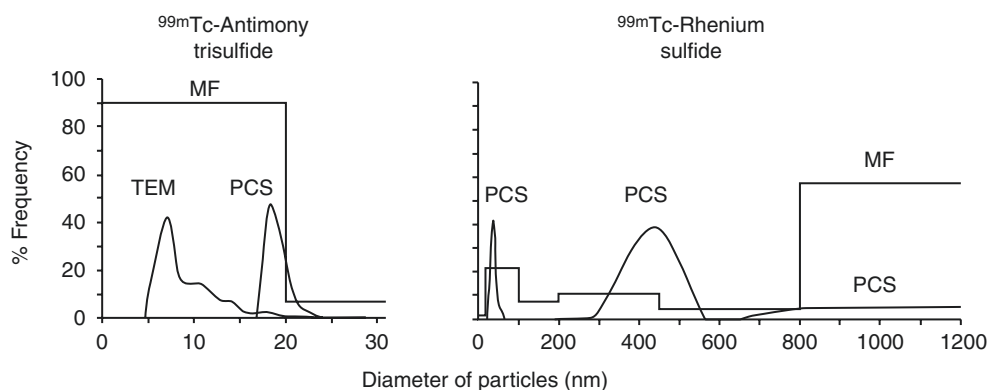
Fig. 3.2 Comparison of transmission electron microscopy (TEM), photon correlation spectroscopy (PCS), and membrane filtration (MF) to characterize size distribution of ^{99m}Tc-antimony trisulfide colloid and ^{99m}Tc-rhenium sulfide colloid (*adapted from Tsopelas C. Particle size analysis of ^{99m}Tc-labeled and unlabeled antimony trisulfide and rhenium sulfide colloids intended for lymphoscintigraphic application. J Nucl Med. 2001;42:460–466*)

small proportion remaining in the first lymph node encountered, therefore resulting in the visualization of additional nodes along the same lymphatic path. Larger particles (>100 nm) are trapped in the interstitial compartment for a relatively long period of time [12]. The fraction of tracer that is phagocytized locally or in lymph nodes increases with increasing size [35]. The smaller the molecule, the less convection influences its transport. Convection of dextrans of similar form, shape, and charge has been found to be significantly faster at a molecular weight of 71 kDa than lighter (3 and 40 kDa) and heavier (2 MDa) dextrans [36]. Albumin is convected three times slower than dextran of similar weight (71 kDa), thus suggesting that both the shape and the uneven distribution of charges in the albumin molecule have a relevant impact on its ability to move through the extracellular matrix.

Thus, similar size molecules can vary in their transport properties. In particular, negatively charged dextrans convect faster than neutrally charged dextran of similar size and shape, demonstrating that negatively charged molecules move more easily through the extracellular matrix. This feature is explained by the fixed negative charge of the glycosaminoglycans in the extracellular matrix. The repelling forces between the negatively charged molecules and the negatively charged extracellular matrix components might reduce mechanical interaction, and thus lower the resistance against convection.

Differences in surface characteristics of the colloids may account for differences in lymph node uptakes [31]. Early studies with liposomes have shown that specific surface properties (such as charge, hydrophobicity, and presence of targeting ligands) can influence both the rate of particle drainage from a subcutaneous injection site and the distribution within the lymphatic system. In rats, for instance, small, negatively charged liposomes localize in lymph nodes more effectively than positively charged vesicles when administered subcutaneously into the dorsal surface of the footpad [37].

These considerations are the main determinants for the selection of the suitable molecules both for peripheral lymphoscintigraphy and for SLN mapping. In fact, when peripheral lymphoscintigraphy is performed to assess and quantify tracer retention in local lymph nodes, the radiopharmaceutical should be characterized by high retention in the lymph nodes, i.e., should have a molecular size that promotes phagocytosis. Conversely, if depot washout techniques are used, smaller tracers that mimic in vivo transport of plasma proteins in the lymphatics (with faster interstitial and lymphatic transport and less local retention) are needed to produce faster and more reliable clearance data [38].

In the case of SLN mapping, the use of small particle size may cause problems to the surgeon in distinguishing between the true SLNs and other radioactive sites. The use of large particles reduces considerably the number of lymph nodes detected along a certain lymphatic pathway. It has been estimated that for a colloid size between 20 and 1000 nm, an average 1.3 lymph nodes are detected, whereas particles with size less than 80 nm show an average 1.7 lymph nodes [39–44]. However, the trend of larger molecules to remain at the injection site and their failure to enter in the lymphatic system may result in delayed or even no visualization of lymph nodes [45]. Therefore, the optimal colloidal size for lymphoscintigraphy is believed to be at least 80 nm and ideally around 200 nm [46].

There are significant advantages of using filtered ^{99m}Tc-sulfur colloid, including its low cost, excellent safety profile, and demonstrated clinical value. Nevertheless, this agent has several disadvantages, including minimal absorption from the injection site (typically <5% is absorbed), especially following subcutaneous administration, whereas intradermal administration is associated with faster absorption and visualization of the cutaneous lymphatics often within 1 min after radiocolloid injection. Even in the absence of beta radiation, the conversion electrons from ^{99m}Tc result in a radiation dose of 1–5 rads/injection site (depending on the volume of the injectate and activity administered).

The slow transit into the lymphatic system requires prolonged imaging times. Furthermore, the unpredictable nature of the absorption and transit can make it very difficult to reliably calculate tracer disappearance rates. ^{99m}Tc-sulfur colloid also requires an acidic pH to retain its stability, which often causes the patient to experience burning pain at the injection site [38]. The large particle size of ^{99m}Tc-sulfur colloid (30–1000 nm) [25] contributes to the minimal absorption and slow transit. An attempt to circumvent these difficulties led to the evaluation of filtered sulfur colloid for lymphoscintigraphy [25]. Utilization of a 0.1 µm filter yielded sulfur colloid with a stable particle size <50 nm. The properties of this filtered colloid are similar to those of antimony trisulfide colloid.

Albumin nanocolloid (Nanocoll®) has a reproducible colloid size distribution (95% of the particles being <80 nm) and ease of labeling. Its rapid clearance from the injection site makes it suitable for quantitative studies, and injections are reportedly painless. Thus, ^{99m}Tc-albumin nanocolloid may be more suitable for quantitative studies than ^{99m}Tc-sulfur colloid.

In addition to radiocolloids, a novel tracer with a retention mechanism in lymph nodes different from that of colloidal particles has recently been approved, both in the United States and in Europe, specifically for SLN mapping. ^{99m}Tc-mannosyl-DTPA-dextran (or ^{99m}Tc-tilmanocept, available commercially as Lymphoseek®) is a small-sized macromolecule with an average diameter equivalent to about 7.1 nm, which consists of a dextran backbone with

multiple units of DTPA and of mannose covalently conjugated with the dextran backbone. The DTPA molecules serve for labeling with ^{99m}Tc, while the mannose residues determine the binding of ^{99m}Tc-tilmanocept to CD206 mannose receptors that are abundantly expressed on the surface of macrophages lining the lymph node sinusoid spaces. Advantages of ^{99m}Tc-tilmanocept versus the radiocolloid tracers commonly employed for SLN mapping include faster clearance from the site of interstitial injection (due to the small size of the agent), and higher retention in the SLN (due to an avid, specific ligand-receptor binding mechanism, which minimizes further migration of the agent to higher tier lymph nodes along the same lymphatic drainage pathway) [47].

Radioactive nanocolloids can also be used for PET, for example nanocolloidal albumin labeled with zirconium-89 (^{89}Zr, with physical decay half-life of 78 h) (Table 3.2) [48]. For the synthesis of this radiopharmaceutical, the precursor from the kit for labeling colloidal HSA with ^{99m}Tc was pre-modified with p-isothiocyanatobenzyl-desferrioxamine B (Df-Bz-NCS) and labeled with ^{89}Zr (Fig. 3.4).

To obtain Df-Bz-NCS-nanocolloidal albumin, polysorbate-citrate buffer (950 μL, pH 6.5) is added to the vial of nanocolloidal albumin (0.5 mg) followed by 45 μL of 0.1 M Na_2CO_3 to reach pH 9, and 167 nmol of Df-Bz-NCS in 20 μL of dimethyl sulfoxide (in 4–5 μL steps). After 30-min incubation at 37 °C, nonconjugated Df-Bz-NCS is removed by size-exclusion chromatography using a PD10 column and

polysorbate-citrate buffer at pH 6.5 as the eluent. Then, 200 μL of ^{89}Zr-oxalate (20–25 MBq) is added to a wobbling reaction vial followed by 90 μL of 2 M Na_2CO_3. After 3 min, the following solutions are added: 300 μL of 0.5 M N-(2-hydroxyethyl)piperazine-N9-(2-ethanesulfonic acid) buffer, pH 7.0; 710 μL of Df-Bz-NCS-nanocolloidal albumin (0.18 mg); and 700 μL of 0.5 M N-(2-hydroxyethyl) piperazine-N9-(2-ethanesulfonic acid) buffer, pH 7.0. The solution is incubated for 60 min at room temperature and then reaction mixture is purified through a PD10 column (eluent: polysorbate-citrate buffer, pH 6.5). No differences were observed between ^{89}Zr- and ^{99m}Tc-nanocolloidal albumin regarding particle size and uptake in the regional lymph nodes, thus indicating that coupling with ^{89}Zr does not alter the physic-chemical properties of nanocolloidal albumin.

3.2.2 Injected Volume and Activity for Lymphatic Mapping

The effects of varying concentrations of the particles and the influence of injected volume and activity parameters on the outcome of lymphoscintigraphy are still unclear. Bourgeois has investigated the effect of variable concentration (0.02 mg versus 0.2 mg) and volume (0.2 mL versus 1.0 mL) of ^{99m}Tc-HSA nanocolloids injected subcutaneously in the foot on lymph node uptake after 1 h during peripheral lymphoscintigraphy. He found that inguinal activity was highest using the highest quantity in the lowest volume [51].

Improvement in the SLN identification rate from 83 to 94% has been demonstrated with a 50% increase of injected activity [52]. Regarding volume of the injectate, because of the non-physiologic increase in interstitial pressure the administration of a large volume of injectate may lead to drainage toward both homoregional non-SLNs and to additional drainage regions [53].

Table 3.2 Radiopharmaceuticals for PET imaging of the lymphatic pathways

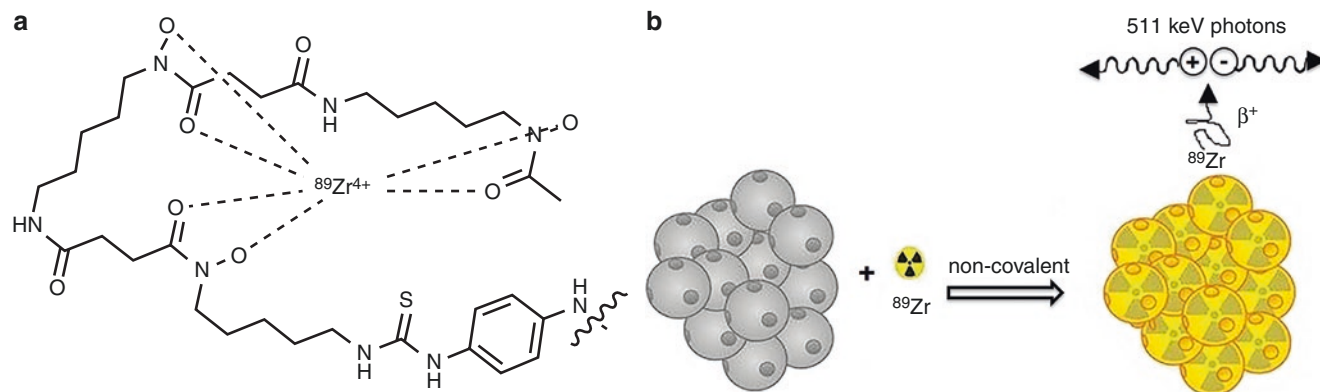| Radiotracer	Half-life	Ref
^{89}Zr-albumin nanocolloid (Nanocoll)	78.4 h	[48]
^{68}Ga-NEB	67 min	[49]
[^{18}F]AlF-NEB	110 min	[50]

Fig. 3.4 Radiolabeling of compounds for lymphatic mapping with different positron-emitting radionuclides. (**a**) Df-Bz-NCS complex with ^{89}Zr^{4+}. (**b**) Radiolabeling of modified nanocolloids with ^{89}Zr

3.2.3　Factors Affecting Radiocolloid Uptake During Lymphatic Mapping

Mechanical massage over the radiocolloid injection site enhances the uptake and weakens the inverse correlation between particle size and speed of lymphatic drainage. Besides the influence of particle surface properties on radiocolloid uptake [31], an increase in venous pressure decreases concentration of macromolecules and leukocytes in the lymph [54]. Particle uptake by the lymphatic system is also temperature dependent. In this regard, protein transport across the canine lymphatic endothelium is enhanced with increasing temperature [55]. In addition to temperature, the pH of lymph or interstitial fluid may also alter lymph or particle uptake/transport. The colloid osmotic pressure of body fluids increases as pH increases (2.1 mmHg per pH-unit) [56]. Whether pH differences in interstitial or lymphatic fluid affect particle uptake in vivo, however, remains to be investigated.

Studies on prenodal collecting lymphatics of the lower extremities have shown that exercise indeed increases lymph flow [57, 58]. The type and intensity of the exercise have an important effect on the lymphatic function, and therefore on the outcome of a lymphoscintigraphic examination (see Chap. 4 for specific stress protocols).

> **Key Learning Points**
> - Following the pioneer studies on lymphatic circulation performed with colloidal [198]Au, the most widely employed agents for lymphatic mapping are colloidal particles labeled with [99m]Tc.
> - The feasibility of lymphatic mapping with ^{18}F or [89]Zr labeling is also being explored.
> - Injected volume and activity affect migration of the lymphatic mapping agents from the site of interstitial administration and their migration through the lymphatic circulation.
> - Other physicochemical and biological factors affect radiocolloid uptake.

3.2.4　Other PET Radiopharmaceuticals for Lymphatic Mapping

PET lymphography has been investigated with intradermal administration of [18F]FDG for combined diagnostic and intraoperative visualization of LNs [59]. Within 30 min after tracer injection, lymphatic vessels and LNs can be clearly revealed by PET in an animal modal. However, the clinical application of [18F]FDG PET lymphography is challenged by the fast migration of the small molecules into blood circulation and it has never been translated into humans.
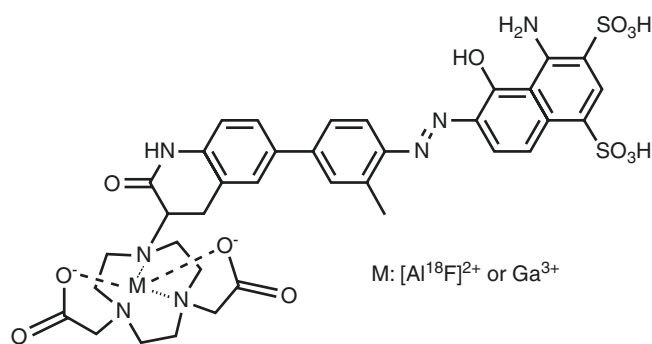

Fig. 3.5 Structure of ^{68}Ga-NEB or Al[18]F-NEB

Recent developments of PET radiopharmaceuticals (Table 3.2) include a truncated form of the azo dye Evans blue (EB) after conjugation via a 1,4,7-triazacyclononane-N,N′,N″-triacetic acid (NOTA) linker (NEB) [60] labeled with either fluorine-18 by the formation of [18F]aluminum fluoride complex ([18F]AlF-NEB) or gallium-68 (^{68}Ga-NEB) (Fig. 3.5). The EB dye has high affinity for serum albumin and has been used clinically to determine blood volume [61]. Although recently discontinued in clinical practice, EB is still used as a sensitive marker of protein leakage from the vascular lumen in a variety of tissues during inflammation and traumatic injury [62]. After intravenous injection, [18F]AlF-NEB complexed with serum albumin quickly, and thus most of the radioactivity remained in the blood circulation. [18F]AlF-NEB has been successfully applied to evaluate cardiac function in a myocardial infarction model and vascular permeability in inflammatory and tumor models [50]; more recent studies have investigated [18F]AlF-NEB along with the EB dye for lymphatic imaging after interstitial injection. ^{68}Ga-NEB synthesis consists of a mixture of ^{68}Ga freshly eluted from a [68]Ge/^{68}Ga generator using HCl 0.05 M and mixed with NaOAc 0.4 M to adjust pH to 4.5, to a vial containing the NEB, shaking, and incubation in a heating block at 95 °C for 10 min. Then, the product requires a passage through a C18 cartridge, elution with 2 mL of 80% ethanol/water, dilution in sterile saline solution, and filtration on a 0.22 μm aseptic filtration membrane. Quality control is performed with HPLC or ITLC, using CH_3OH:NH_4OAc (v/v 1:1) as eluent [50].

After a mean injected dose of 139.5 ± 10.36 MBq (3.77 ± 0.28 mCi), PET images acquired at 30 min after intravenous administration showed cardiac ventricles, major arteries, and veins. The liver, spleen, and kidneys are also visible, with relatively low activity, whereas the bladder showed high activity, increasing over time. Although the blood vessels in the brain showed high radioactivity, the normal brain tissue had negligible accumulation of ^{68}Ga-NEB, indicating that the tracer does not cross the blood–brain barrier. The mean absorbed radiation doses based on multiple-
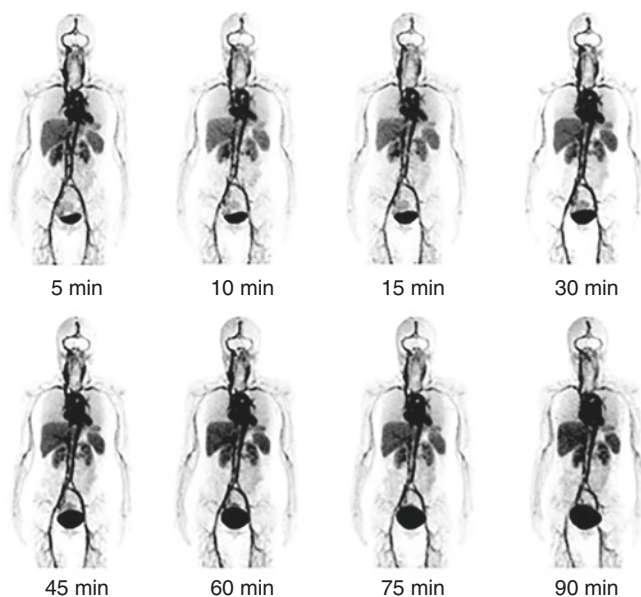
Fig. 3.6 Multiple-time-point whole-body maximum-intensity-projection PET images of a healthy woman at 5, 10, 15, 30, 45, 60, 75, and 90 min after intravenous administration of ^{68}Ga-NEB (*reproduced with permission from ref:* [63])

time-point PET revealed that the organs receiving relatively high doses were the kidneys, liver, spleen, and heart wall. The bladder wall also received high exposure due to renal excretion of the radioactivity (0.0683 ± 0.0090 mSv/MBq). The whole-body absorbed dose was 0.0151 ± 0.0001 mSv/MBq, with an effective dose of 0.0179 ± 0.0003 mSv/MBq. Upon PET/CT imaging, the LNs and lymphatic vessels as well as other desired tissues can be visualized, as shown in Fig. 3.6 [63].

After local administration, NEB forms a complex with albumin in the interstitial fluid and travels through the lymphatic system. Therefore, for the study of patients with lymphedema subcutaneous injection can be performed (see Chap. 4 for specific protocols).

Key Learning Points
- Newer perspectives for PET imaging of lymphatic circulation are based on the use of new radiopharmaceuticals including a truncated form of the azo dye Evans blue (EB) to be labeled with ^{68}Ga or ^{18}F, after conjugation via a 1,4,7-triazacyclononane-N,N′,N″-triacetic acid (NOTA) linker (NEB).
- The synthesis of ^{68}Ga-NEB and [^{18}F]AlF-NEB has been validated.
- Initial studies describe the biodistribution of NEB derivates in animal models as well as in humans, as evaluated by PET imaging.

3.3 Iodine-Based CT Contrast Agents for Lymphatic Mapping

In order to achieve higher levels of X-ray attenuation than those observed for biological tissue, elements of higher atomic number (Z) are incorporated into the contrast agent molecule. Iodine (Z = 53; M = 127) has historically been the atom of choice for CT imaging applications [64]. Sodium and lithium iodide were among the first water-soluble imaging agents. However, due to the associated toxicity at the iodine concentrations necessary for imaging they are not suitable for most clinical applications. Consequently, covalently bound iodine provides a better option in contrast media design.

Small-molecule iodinated contrast agents can be classified into two main categories: the "ionic" and "nonionic" molecules. Most ionic iodinated contrast agents studied to date are negatively charged species. Although widely used in the clinical routine, these ionic iodinated imaging agents possess several inherent disadvantages compared to nonionic contrast media.

Currently used contrast media exhibit high water solubility, low binding to biological receptors, low toxicity, and high bio-tolerability. A number of such contrast agents (both ionic and nonionic, and mono- and two-ring structures) are approved for medical use and clinically used worldwide (Table 3.3 and Fig. 3.7).

After i.v. injection, a contrast medium travels to the right heart, the pulmonary circulation, and the left heart before reaching the central arterial system. Contrast medium rapidly redistributes from the vascular to the interstitial spaces of the organs. Since iodinated contrast media consist of relatively small molecules that are highly diffusible, the transport of contrast media is predominantly "flow limited" and far less "diffusion limited." In a flow-limited process, the delivery of contrast medium through the circulatory system to an organ is a crucial determinant of contrast enhancement [65]. Well-perfused organs such as the kidney, the spleen, and the liver show high contrast enhancement during the initial circulation (first pass) of contrast medium to the organs. Contrast material-enhanced blood recirculates (normal recirculation may range in 15–40 s) and may contribute to the overall pattern of contrast enhancement achieved at CT imaging acquisition. For relatively long i.v. infusions, recir-

Table 3.3 Some common commercially available small-molecule iodinated contrast agents and their indicated clinical uses [64]

Common name	Commercial name	Manufacturer
Iohexol	Omnipaque™	GE Healthcare
Iopromide	Ultravist™	Bayer Healthcare
Iodixanol	Visipaque™	GE Healthcare
Ioxaglate	Hexabrix™	Mallinckrodt Imaging
Iothalamate	Cysto-Conray II™	Mallinckrodt Imaging
Iopamidol	Isovue™	Bracco Imaging

Fig. 3.7 Common iodinated contrast agents: (**a**) iohexol; (**b**) iopromide; (**c**) iodixanol; (**d**) ioxaglate; (**e**) iothalamate; (**f**) iopamidol
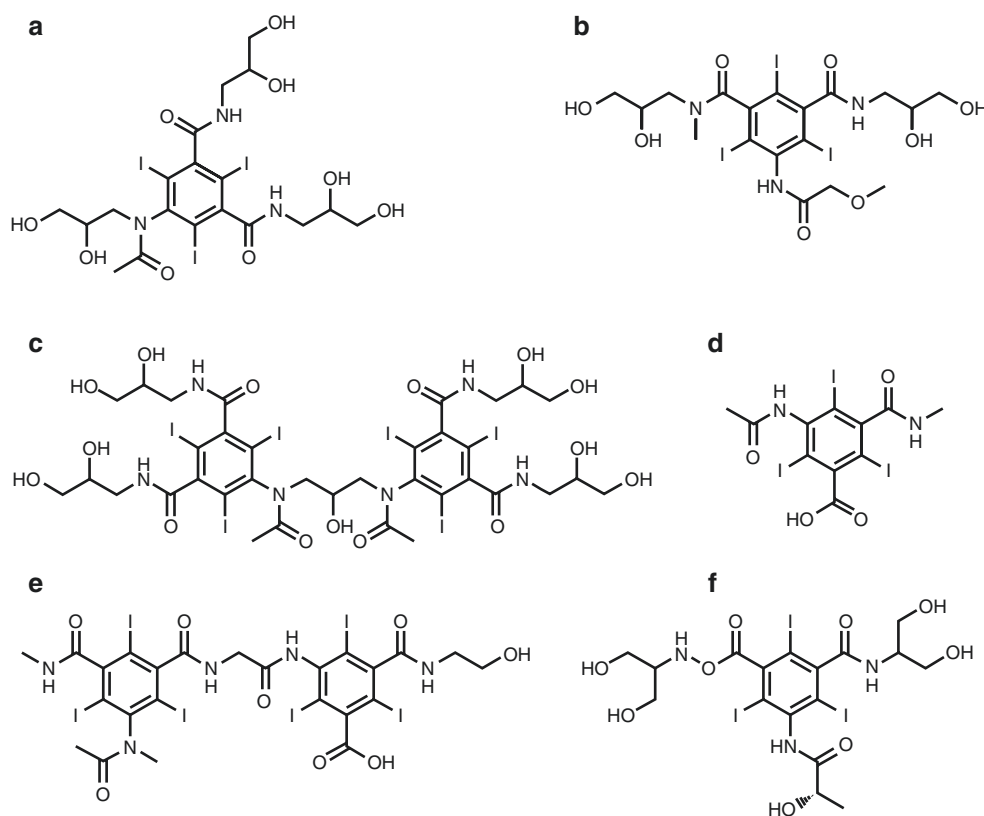
culation can even occur during the infusion of the contrast material [66].

Contrast enhancement at CT is affected by numerous interacting factors: patient (i.e., patient body size, cardiovascular circulation time, age, sex, venous access, renal function, hepatic disease), type and modality of contrast medium administration (i.e., duration of injection, injection rate, shape of injection bolus shape, contrast medium volume, concentration, physicochemical properties, use of a saline flush), and CT scanning. Contrast medium pharmacokinetics and contrast enhancement are determined solely by the patient and contrast medium factors and are independent from the CT scanning technique. Nevertheless, CT scanning factors play a critical role by allowing us to acquire contrast-enhanced images at a specific time point of contrast enhancement.

While current clinically approved small-molecule iodinated CT contrast agents offer safety and imaging efficacy, they do suffer from several drawbacks, which prevent them from being used for all applications:

- Nonspecific biodistribution.
- As small-molecular-weight molecules, they tend to undergo rapid renal clearance.
- High osmolality and/or high viscosity of the contrast media formulations can lead to renal toxicity [67–69] and/or adverse physiological effects [70–72].
- High "per-dose" concentrations are required.

- High rates of extravasation and equilibration between intravascular and extravascular compartments at the capillary level often make it difficult to obtain meaningful and clear CT images [73–75].

Contrast agents can access the lymphatic system by three different routes: intravenous, intralymphatic (direct lymphatic injection), or interstitial. Contrast agents for direct intralymphatic injection are not being developed due to the inherent difficulties in finding and cannulating the lymphatic vessels. Thus, the newer contrast agents tend to follow the other two routes. Methods developed for cancer imaging may well have application in other diseases affecting the lymphatics.

An iodized oil-in-water emulsion in which lipiodol was emulsified by a surfactant mixture (Tween 80 as the main surfactant and TPGS, Kollidon 12 PF, or Span 85 as the co-surfactant) was investigated in a preclinical study, showing that all the three types of emulsions formulated with different co-surfactants exhibited similar mean particle sizes (approximately 120–130 nm), and they were all effectively taken up in the targeted lymph node without significant differences in the mean values of peak Hounsfield units (HU), time to peak HU, and sustained enhancement duration. Lymph nodes showed peak enhancement 4–8 h after injection with sustained contrast enhancement, which means that the time window for CT can be expanded, in comparison with CT lymphography, using iopamidol. In addition, the compound was completely

eliminated on delayed CT imaging, in contrast with lipiodol. CT lymphography using lipiodol showed continuously increased attenuation values even after 1 week [76].

In dogs, at lower injection volumes (0.1–0.5 mL), uptake of contrast material in target lymph nodes appeared incomplete, although the node was still well visualized. When larger volumes (2–4 mL) of contrast material were injected, marked opacification of target nodes occurred with good definition of lymph node margins. The dose response to iodinated particles injected subcutaneously or submucosally is predictable in terms of total iodine uptake and as measured by attenuation (HU) or iodine concentration in normal lymph nodes. Within the imaging time range evaluated, peak enhancement of lymph nodes appears to occur between 12 and 24 h after injection of contrast material. In cancerous lymph nodes, although nodes with greater than 25% tumor replacement were larger and had a higher total iodine uptake per node, node opacification (as expressed in HU or milligrams of iodine per cubic centimeter of lymph node tissue) was less than that in normal nodes and in lymph nodes with 25% or less tumor replacement. In addition, characteristic architectural alterations, including changes in the cortex, medulla, and cortico-medullary junction that resulted from the presence of tumor deposits, were useful in distinguishing between normal and cancerous lymph nodes [77]. In patients with breast cancer, 2 mL of iopamidol was administered into the two skin areas (the border between the upper medial and lateral quadrants, and the border between the lower medial and quadrants) overlying the left mammary gland, dividing the volume equally to identity SLNs. The exact mechanism(s) of iopamidol uptake and transport in the lymphatic system is still unknown. This agent appears to penetrate easily into the lymphatics through the clefts in the terminal lymphangioles of the interstitial space, as with other water-soluble, low-molecular-weight solutes. The relatively long duration of the nodal enhancement may be related to slow transit and sequestration of iopamidol in the lymph node sinusoid spaces.

Key Learning Points
- Iodine-based CT contrast agents can be classified into two main categories: the "ionic" molecules and the "nonionic" molecules.
- Biodistribution of iodinated contrast agents varies according to various factors that affect their binding to plasma proteins and/or to other endogenous compounds.
- High-viscosity iodinated contrast agents are being investigated as to their ability to explore the lymphatic structures and circulation.
- There are well-known drawbacks in the use of iodinated contrast media that should always be considered before administration to patients.

3.4 MR, MRL, and PET/MRI Contrast Agents for Lymphatic Mapping

The MRI signal arises from the excitation of low-energy nuclear spins, which occur in a permanent magnetic field by applying radiofrequency pulses followed by measurement of the spin relaxation processes (i.e., T1 recovery or T2 decay). Different chemical environments as well as water concentration result in different signal strengths and therefore provide contrast between fat, tissue, and bones. Paramagnetic compounds can be used to enhance the contrast of MR images by promoting relaxation of water near the compound. MRI contrast agents are classified as either T1 (i.e., positive) or T2 (i.e., negative).

The contrast agents in clinical use are low-molecular-weight Gd^{3+}-based complexes (0.5–1 kDa) with one molecule of water in the inner sphere [78] and relaxivity ranging from 3 to 5 mM/s at 1.5 or 3 T (clinical magnetic fields).

The macromolecular contrast agent albumin–gadolinium diethylenetriamine penta-acetic acid (albumin-Gd-DTPA) consists of human serum albumin to which paramagnetic properties are conferred by covalent binding from 9 to 18 Gd-DTPA-chelates per protein molecule. Whereas Gd-DTPA distributes from the intravascular to the extravascular space and is rapidly cleared from the body through renal excretion [79], making it unfavorable as a blood pool agent, albumin-Gd-DTPA shows high relaxivity and remains largely confined to intravascular spaces [80, 81]. This compound has been used to quantify delivery, transport rates, and volumes of macromolecular fluid flow through the interstitial-lymphatic continuum in tumors [82].

Intracutaneous injection of extracellular, paramagnetic contrast agents has recently been proposed for identifying abnormal lymphatic pathways by MR lymphography (MRL) [83–85]. These agents include Gd-labeled dendrimers [86, 87], macrocyclic Gd complexes [83], and Gd-labeled dextran [88] (Table 3.4 and Fig. 3.8).

Table 3.4 Main features of Gd-based contrast agents with potential use of MR lymphography

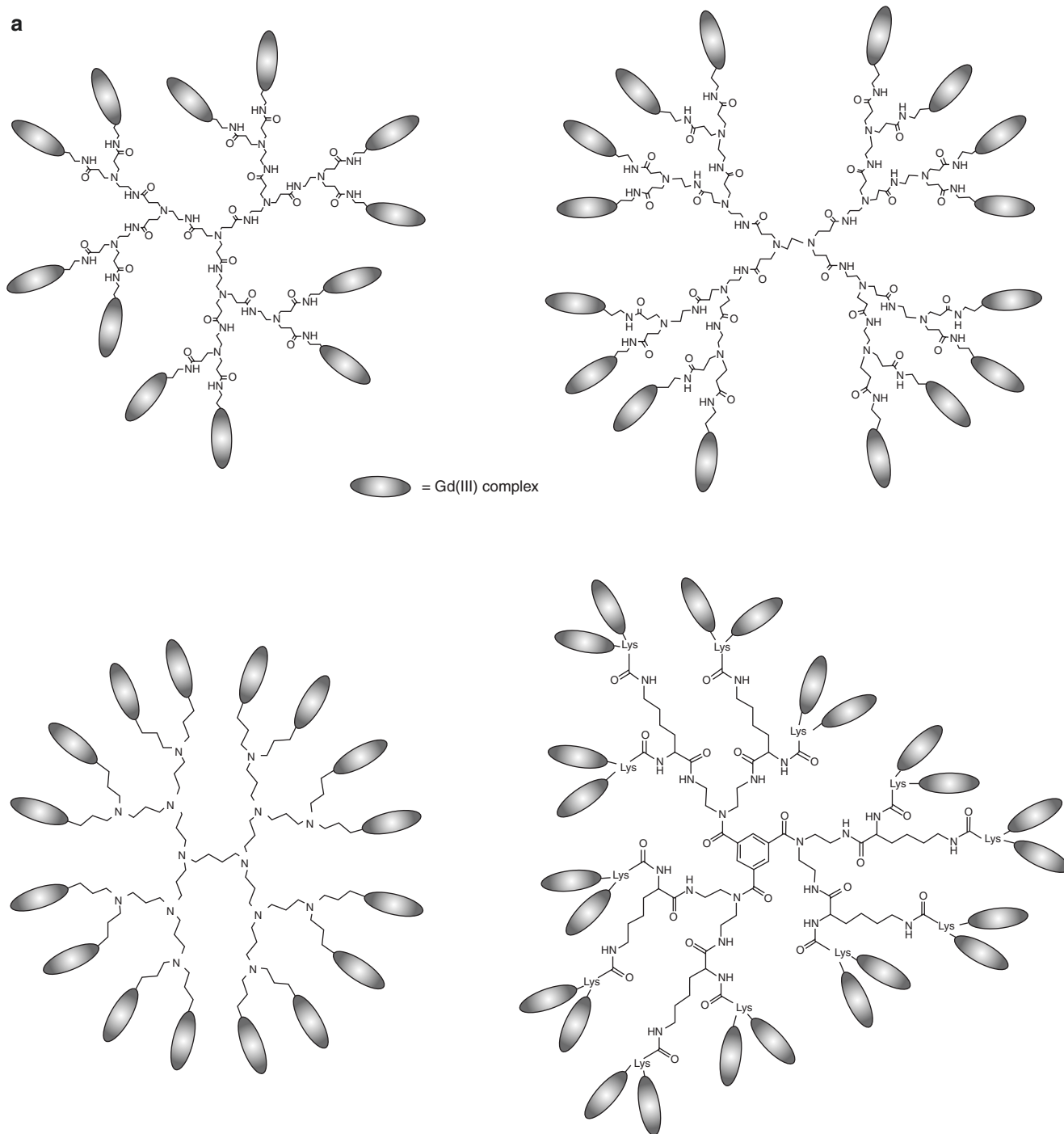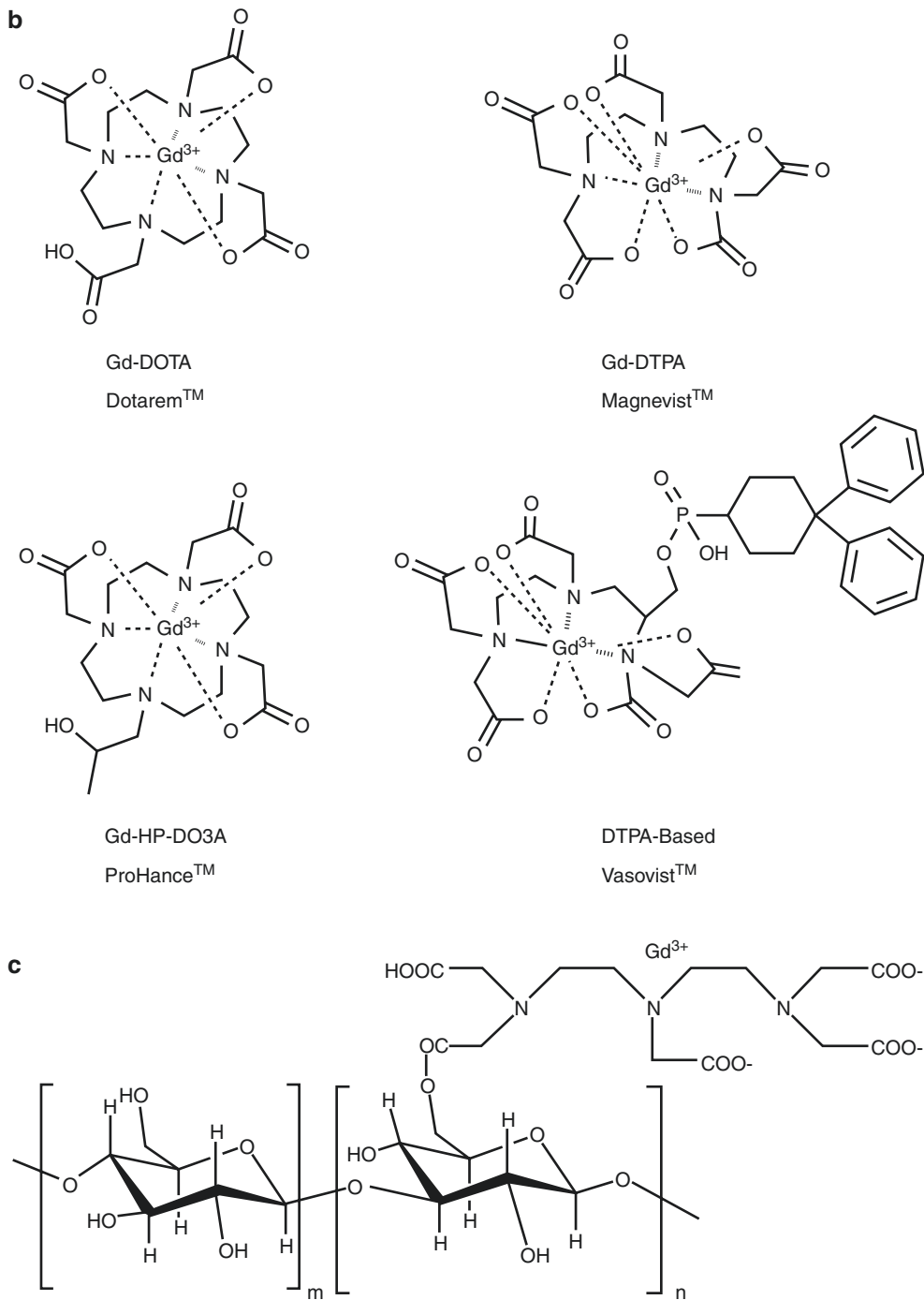| Contrast agent	Enhancement and physicochemical effect	References
Gd-DOTA	Positive-ionic-macrocyclic	[78, 89]
Gd-DTPA	Positive-ionic-linear	[78, 90]
Gd-DTPA-BMA	Positive-ionic-linear	[91]
Gd-HP-DO3A	Positive-ionic-macrocyclic	[92]
Gd-DTPA-BMEA	Positive-ionic-linear	[93]
Gd-DO3A-butrol	Positive-ionic-macrocyclic	[78]
Gd-BOPTA	Positive-ionic-linear	[78]

a

= Gd(III) complex

Fig. 3.8 Most common Gd complexes used as MRI contrast-enhancement agents. (**a**) Gd-labeled dendrimers. (**b**) Macrocyclic Gd complexes. (**c**) Gd-labeled dextran (*reproduced with permission from ref.* [78])

b

Gd-DOTA
DotaremTM

Gd-DTPA
MagnevistTM

Gd-HP-DO3A
ProHanceTM

DTPA-Based
VasovistTM

c

Fig. 3.8 (continued)

3.4.1 Dendrimers for Lymphatic Mapping

This definition identifies a family of synthetic monodispersed polymers that can be produced at predefined and chemically identical sizes. Two forms of dendrimers are commercially available: poly-amidoamine (PAMAM) and diaminobutane-core poly-propylimine (DAB or PPI). Different generations (sizes) of dendrimers have been investigated as MRL macromolecular contrast agents. Kobayashi et al. used interstitially injected generation-6 (G6) PAMAM dendrimers to image the lymphatic system and SLNs in normal mice and in mice with xenografted breast tumors [94]. G6 was injected directly into the mammary gland or peritumorally, and three-dimensional reconstruction was used to aid anatomical localization. The same group used a similar contrast agent in a mouse lymphoma model [95]. They were able to differentiate normal and abnormal lymphatics and to distinguish intralymphatic from extra-lymphatic disease. Kobayashi et al. also compared MRL with either PAMAM dendrimers of different generations or less hydrophilic DAB generations in murine models [86]. PAMAM-G8 was retained in the fine lymphatic vessels without major leakage, thus resulting in excellent imaging of the lymphatic channels. However, PAMAM-G4 provided a better contrast of lymph nodes that were close to the liver, due to a reduced background signal. DAB dendrimers are expected to clear more rapidly from the circulation due to their uptake and excretion by the liver and kidneys. Indeed, DAB-G5 was cleared more rapidly from the lymphatic vessels, but retained in the lymph nodes. Therefore, PAMAM dendrimers may perform better for imaging the lymphatics, while DAB dendrimers are more optimal for lymph node imaging.

Another interesting advance in lymph node imaging is the use of dual-modality contrast agents. Talanov et al. synthesized a PAMAM G6 dendrimer conjugated to gadolinium for MRL and to the cyanine derivative Cy5.5 for optical imaging [96]. The agent was injected into the mammary fat pad of mice and SLNs were successfully imaged on MRI, followed by similarly successful optical imaging.

3.4.2 Superparamagnetic Iron Oxide Particles (SPIONs and USPIOs) for Lymphatic Mapping

Superparamagnetic iron oxide nanoparticles (SPIONs) [97] are single-domain magnetic iron oxide particles with hydrodynamic diameters ranging from single nanometers to >100 nm [98–100]. SPIONs are typically classified into three categories based on their hydrodynamic diameter: (1) oral (large) SPIONs at 300 nm–3.5 μm, (2) standard (regular) SPION (SSPIO) nanoparticles at 50–150 nm, and (3) ultrasmall SPIO (USPIOs) nanoparticles less than 50 nm [99, 100].

Larger SPIONs exhibit higher nonspecific uptake by the mononuclear phagocyte system or reticuloendothelial system than smaller USPIOs, which indicates a higher percentage of passive uptake of larger particles for tissues rich in macrophages, such as the liver, spleen, lymph nodes, or bone marrow [99]. Faster biodegradation rates in the liver and spleen have been recently reported for monodisperse 5 nm iron oxide cores in comparison with 15 and 30 nm iron oxide cores coated with the same coating molecules [101].

SPIONs can be monodisperse and coated with biologically compatible ligands, are chemically and biologically stable [102], and are generally nontoxic in vivo [103]. However, commercially available SPION contrast agents are composed of polydisperse inorganic cores ranging from ~16 to ~200 nm. Generally, large SPIONs function as T2 contrast agents, whereas small SPIOs have limited T2 activity and therefore are potential T1 contrast agents. In addition, the large size of existing SPIONs [104] prevents their efficient renal clearance after i.v. administration, thus greatly differing from GBCA as to their clearance pathways. As a result, large HD SPIONs predominantly accumulate in the body [105] and can cause a persistent negative contrast over several weeks or months, which prevents repeated imaging studies and limits the clinical management of patients. Furthermore, current SPION formulations are almost quantitatively metabolized and absorbed into the iron pool, thus potentially causing clinical side effects due to iron overload [105].

USPIOs are macromolecular MR contrast agents with a long serum half-life that can be utilized for systemic lymph node imaging. Following intravenous injection, they are phagocytosed by circulating macrophages and transported to the lymph nodes. Clustering of the iron oxide particles within these phagocytic cells produces local field inhomogeneities and results in decreased signal intensity on T2- and T2∗-weighted images [106]. The pharmacodynamics of USPIO dictates that the optimal time for imaging is 24–36 h after administration. Anzai et al. have shown that the dose of USPIO administered affects the degree of signal reduction [107]. They injected dose ranges of 0.3–1.7 mg Fe/kg in five healthy volunteers. The 1.7 dose produced the greatest signal decrease on T2∗-weighted imaging. Further studies have suggested that a higher dose of 2.6 mg Fe/kg performs even better. However, the higher concentrations of iron within the lymph node may mask small intranodal tumor cell foci [108]. The translation of these macromolecules into clinical application is restricted by delayed renal clearance and uptake into the reticuloendothelial system. Furthermore, interstitial MRL with commercially available extracellular Gd chelates is markedly limited by nonspecific distribution. In fact, the contrast agents circulate and then freely distribute in the

extracellular space. Extracellular fluid agents are mainly eliminated by renal excretion. Gadolinium enters the liver through the hepatic artery and portal vein, and is freely redistributed into the interstitial space. In contrast to iodine molecules, which are imaged by CT, the effect of gadolinium is assessed by MR imaging rather than by imaging the molecule itself. Gadolinium exhibits an amplification effect, because several adjacent water protons surrounding a gadolinium atom are relaxed.

Despite the promise of MMCMs for use in MRL, USPIOs are the only agents that have been investigated in humans. Iron oxide-based contrast agents seem ideally suited to lymph node imaging when used for staging purposes. However, for SLN mapping, interstitial injection of Gd-based macromolecules, such as dendrimers, seems to be a superior choice.

> **Key Learning Points**
> - Contrast agents for MR imaging, MR lymphography, and PET/MRI are described in this section.
> - Gadolinium contrast agents for MRI include Gd-labeled dendrimers, macrocyclic Gd complexes, and Gd-labeled dextran.
> - The use and biodistribution of superparamagnetic iron nanoparticles as MR contrast agents are described in this section.

3.5   Contrast-Enhanced Ultrasound Imaging for Lymphatic Mapping

Contrast-enhanced ultrasound (CEUS) using microbubbles has been widely used both in preclinical experiments and in the clinical setting [109–116]. Microbubbles are gas-filled particles with an average diameter of several micrometers (Fig. 3.9). Microbubbles larger than red blood cells (RBCs) would be trapped in the capillaries, and submicron-size microbubbles scatter ultrasound poorly and have insufficient stability. During ultrasonography, the energy pulses generated by the transducer array cause rapid variations of pressure (up to several megapascals) in tissues. Therefore, microbubbles in blood undergo volume oscillations at clinical diagnostic ultrasound imaging frequencies (1–15 MHz). Microbubbles vibrate, resonate, and re-emit sound, and resulting backscatter ultrasound signal is detected. The re-emitted ultrasound contains signal at harmonic frequencies [118]. Sensitive microbubble detection relies on the ability of the imaging system to differentiate bubble backscatter signal from tissue background. Modern ultrasound imaging techniques can depict individual bubbles with particle mass less than 1 pg [119]; hence the required mass of ultrasound
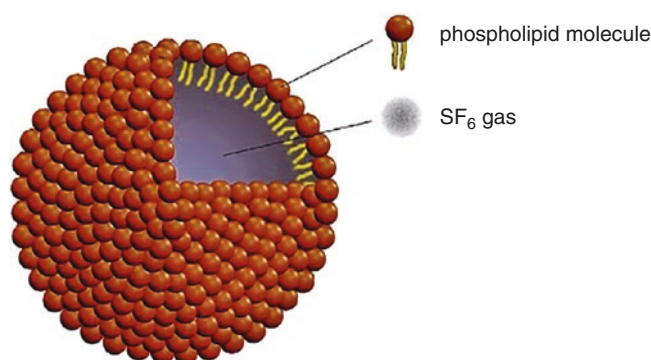

Fig. 3.9 General structure of microbubbles (*reproduced with permission from ref* [117])

contrast material is low, comparable with the dose of some nuclear medicine agents. For clinical enhancement of the blood pool, a microbubble contrast aqueous dispersion volume of 0.1–5 mL (concentration ≈109 bubbles/mL) is routinely injected or infused i.v.

Once administered i.v., micron-size bubbles circulate in the bloodstream for minutes [120]. The bubble clearance mechanism is different from clearance of other types of microparticles and nanoparticles, in that gas is cleared through gas exchange via expiration by the lungs. For example, within 6 min after i.v. administration of perflutren (Optison), 99.9% of C_3F_8 is exhaled. Residual microbubble shell material and some intact bubbles are cleared by phagocytosis (the rate of this process depends on the bubble shell material and PEG coat) [121]. The major sites for microbubble accumulation are the liver (Kupffer cells) and spleen (macrophages) [122, 123].

Ultrasound contrast agents are generally considered safe, since serious adverse events have been reported very rarely [124]. In 2007, the U.S. Food and Drug Administration (FDA) introduced a "black box" warning for microbubble use owing to the risk of serious cardiopulmonary reactions in some patients. The warning was later relaxed because it was recognized that the rate of adverse reactions of microbubbles is comparable to or lower than that of other types of contrast agents [125], and use of microbubbles does not affect mortality in an undesired way [126].

In preclinical studies, microbubbles have been shown to accumulate in SLNs but not in second-tier lymph nodes, probably due to the avidity of macrophages for the shell material [127, 128]. In a pilot clinical trial, patients with breast cancer received a periareolar intradermal injection of microbubbles preoperatively, lymphatic channels were visualized immediately by ultrasonography, and putative axillary SLNs were identified. The sensitivity of SLN detection in this study was 89% [129]. Similar to MRI, differentiation of benign and malignant lymph nodes can be achieved with CEUS because of the different accumulation of microbubbles in normal and metastatic LNs [130]. Several limitations

of CEUS prevent broad application of this technique for SLN mapping, such as poor spatial resolution, slow migration of the microbubble, inaccessibility to ultrasound exploration of the thorax and deep retroperitoneum, as well as its dependence on operator experience [131].

Photoacoustic imaging (PAI) is a hybrid imaging modality based on the detection of the ultrasonic waves generated by pulse laser-induced transient thermoelastic expansion within biological tissues [132–135]. In combination with different contrast agents including methylene blue, carbon nanotubes, gold nanocages, gold nanorods, and gold nanobeacons [136–139], PAI showed potential for improved detection of metastases in preclinical models. However, no clinical application has been reported so far, possibly due to the lack of bedside imaging system. In addition, the still limited signal penetration and challenges in control of the surgical field with conductive gel currently constitute serious drawbacks of this imaging technique.

> **Key Learning Points**
> - Microbubbles used for contrast-enhanced ultrasound imaging are described in this section.
> - The biodistribution of microbubbles used for contrast-enhanced ultrasound imaging is described in this section.
> - Microbubbles for contrast-enhanced ultrasound imaging are being employed in preclinical and clinical trials as lymphatic mapping agents.

3.6 Optical Imaging Agents for Lymphatic Mapping

Optical imaging is a rapidly advancing branch of medical imaging. The method does not imply radiation exposure, although the main advantage of optical imaging lies in its high resolution and its ability to image at a molecular level.

Substances that absorb light energy change to an unstable excitation state from the ground state and then revert back to the ground state after energy transition. This energy transition includes vibrational energy, heat energy, and light energy (fluorescence). A substance that selectively absorbs light of a certain wavelength is called a chromophore. When it emits fluorescence after absorption of excitation light, it is called a fluorophore. In most cases, fluorescent light has lower energy and a longer wavelength than the excitation light, since fluorophores release a certain amount of energy in the form of vibrational relaxation before photoemission. Some fluorophores can be administered into the body to act as a kind of imaging contrast medium; these fluorophores are called exogenous fluoro-
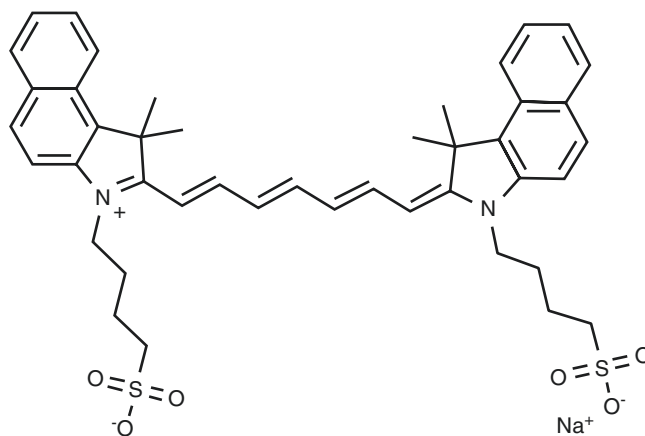

Fig. 3.10 Chemical structure of indocyanine green (ICG)

phores. The body intrinsically emits fluorescence, as many components of the body exhibit weak fluorescence (autofluorescence); these components are called endogenous fluorophores. Organic fluorophores include fluoresceins, rhodamines, and most cyanines. Among the many kinds of fluorophores, fluorescence tracers for biological application are limited to biomolecules that emit near-infrared (NIR) spectrum wavelengths to minimize autofluorescence and improve signal-to-background ratios. Hemoglobin, muscle, and fat are least absorbent in this light range, thus allowing deeper tissue penetration of photons [140].

Currently, the U.S. FDA-approved fluorescent contrasts include only fluorescein and indocyanine green (ICG) (Fig. 3.10). Newer organic fluorophores, including sulfonated indocyanine dyes (e.g., Cy 7), sulfonated carbocyanine dyes (e.g., Alexa Fluor 750), and sulfonated rhodamine dye (e.g., Alexa Fluor 633), are synthetic fluorescent dyes with better optical characteristics and are more photostable and brighter than the preexisting original dyes [141]. Fluorescent probes are safe and they can be conjugated to antibodies, peptides, or proteins as optimal lymphatic tracers due to their small size. Since the conjugations of fluorophore and macromolecules may have a toxicity profile different from its original components separately, their toxicity must be validated before clinical application. Furthermore, the optimal fluorescent signals are still insufficient to provide adequate image quality as compared to inorganic fluorophores, although their fluorescence is more intense than fluorescein or ICG. The main disadvantage remains the poor depth sensitivity of the technique, since penetration beyond 1–2 cm is currently unrealistic; this factor mainly limits its use to animal studies or to human applications that require only superficial imaging (e.g., SLN imaging).

ICG is an amphiphilic, tricarbocyanine iodide dye (mass = 751.4 Da) that is reconstituted in aqueous solution of pH 6.5 for intravenous injection. ICG was introduced as a blood pool agent to measure cardiac output and was

granted FDA approval in 1959 [142]. Intravascularly, the compound binds to plasma proteins that confine most of the bolus to the intravascular space until hepatic uptake and excretion into bile (with clearance rate of 18–24% per minute by the liver) [143]. The plasma proteins, notably serum albumin and α- and β-lipoproteins, bind to the lipophilic component of ICG by the hydrophobic regions of the proteins [144]. This interaction does not alter the protein structure but produces a nontoxic interface and decreases extravasation of the dye [145]. Plasma proteins compete with the tendency of the dye to aggregate in the blood; protein binding leads to the formation of ICG monomers from aggregates in an attempt to establish equilibrium [145]. Of the injected ICG, 98% is bound to plasma proteins while the remaining 2% is free in the serum. Free ICG is then excreted into the bile by glutathione S-transferase, while bound ICG remains within the intravascular space for a longer period [146].

While occupying the intravascular space, the continuing decomposition reaction of ICG releases singlet oxygen molecules that bind to the breakdown products and thermally decompose into carbonyl compounds of low toxicity. Since the singlet oxygen remains within the ICG system, the dye has an LD_{50} (50% lethal dose) of 50–80 mg/kg. With a standard dose of less than 2 mg/kg, ICG is virtually nontoxic, provided that the patient does not suffer from allergy to iodide. The quick clearance rate allows the dye to be used for multiple injections during a procedure, thus being advantageous over other similar substances such as the clinical dye bromsulfthalein [147]. In general, ICG is regarded as safe; however, caution should be adopted in patients with renal failure [148]. Although ICG appears dark green under natural light, it appears more fluorescent than green once injected into the human body in amounts <20 mg [149]. The molecule is generally excited between 750 and 800 nm, and fluorescence is viewed around the maximum peak of 832 nm [143].

Although ICG interacts with plasma proteins, its tendency toward aggregation must be considered to set appropriate parameters for its application. For intravenous injection, water is the desired solvent as the sulfate group of ICG promotes its solubility, while saline solution promotes aggregation of the molecule. The concentration of the dye must be kept below 15 mg/L in the body when used for fluorescent studies, because at higher concentrations it begins to aggregate as a result of van der Waals attractions [144]. In addition to aggregation properties, ICG is relatively unstable before injection and is weakly fluorescent compared with alternative agents. The aqueous solution for injection has limited stability, especially when exposed to light, and must be used within 6–10 h after dilution [143]. As a result, ICG is produced and distributed as a powder for medical applications to reduce its decomposition before use.

Recent advances of nanotechnology have led to the development of quantum dots (QDs). A QD is a nano-sized crystal composed of semiconductor materials (Fig. 3.11). When QDs absorb enough light energy to cause an electron to leave the valence band and to enter the conduction band, an electron-hole pair is produced. During the recombination process between the electron and the hole, light is emitted [19, 28]. The emission wavelength is closely associated with both the composition and size of the QD. As a consequence, the wavelength is dependent on the particle size when the material that makes up QDs is the same. Therefore, by changing the size of QDs, various emission wavelengths can be simultaneously produced by a single-excitation light pulse, a property which enables multiplexed biological imaging. Advantages of QD over conventional fluorophores include a wider excitation range, a sharp and nearly symmetrical emission peak, higher quantum yields, greater penetration depth, longer photostability, and resistance to photobleaching (due to their inorganic composition) [151, 152].

An in vivo multicolor lymphatic imaging technique with QD has been successfully employed in animal models [153]. Kim et al. used type II QD, coated with polydentate phosphine to allow solubility and serum stability in mouse and pig models [154]. A 400 pm concentration of quantum dots was injected intradermally for SLN imaging. This method of SLN lymphog-

Fig. 3.11 Schematic representation of the structure and chemico-physical properties of a quantum dot (QD) (*reproduced with permission from ref* [150])

Core   Shell   Ligands   QD core/shell
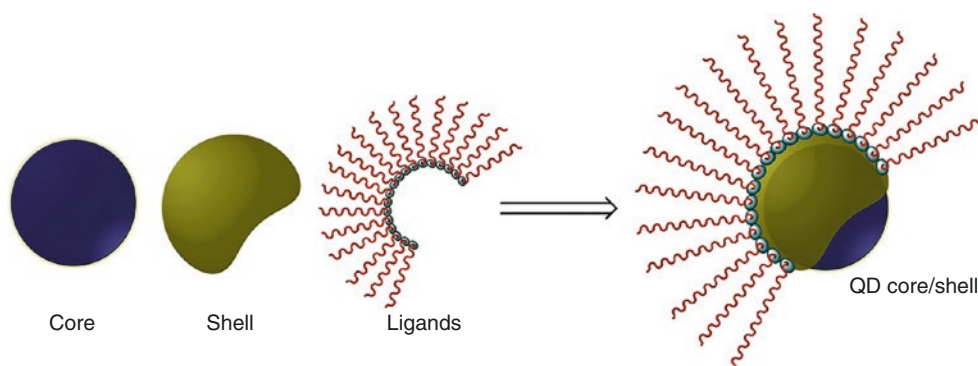
raphy was then shown to be equivalent to the traditional "blue dye" method, showing lymph nodes up to 1 cm deep, along with the lymphatic vessels. This technique may also allow more accurate fluorescence analysis of SLNB specimens.

A critical limitation of QD technology is its potential toxicity, since many of the current-generation QDs are based on a cadmium-selenium core. However, newer, more biocompatible high-yield fluorescent nanoparticles are being developed [155]. The size of QDs makes them ideal candidates for imaging the lymphatic system following interstitial injection. Hama et al. have shown the ability of fluorescence lymphangiography using two NIR QDs with different emission spectra to visualize two separate lymphatic flows that drain into a common nodal basin [153]. Two QDs with emission peaks of 705 and 800 nm were injected simultaneously into the mouse mammary fat pad and the middle phalanx of the upper extremity, respectively. The lymphatics were successfully imaged as they drained into the axillary lymph nodes. This technique could offer SLN detection while concurrently predicting the likelihood, or potential avoidance, of lymphedema following subsequent treatment. Padera et al. have demonstrated the use of multiphoton laser scanning microscopy (MPLSM) to obtain images of deep lymphatic vessels [156]. MPLSM uses a solid-state laser to produce photons in pulses, and a computer-controlled scanning mirror for detection. The light produced is in the infrared spectrum; thus the photons are of a longer wavelength than confocal laser scanning microscopes, and are, therefore, less damaging to tissues and able to achieve greater depth penetration. Padera et al. showed an increased ability to quantify lymphatic size and were able to accurately calculate the density of angiogenic vessels. Leu et al. have shown the reliability of optical imaging techniques in humans. They compared 16 patients with systemic sclerosis with 16 age-matched controls. Imaging of the fingers demonstrated evidence of lymphatic microangiopathy in the affected skin of systemic sclerosis patients [157]. The advances summarized above, along with the development of newer biocompatible fluorescent markers, might in the future allow optical techniques to be more widely used in patients.

Key Learning Points
- Indocyanine green (ICG) and quantum dots (QD) are used as optical imaging agents.
- Upon intravenous administration, ICG interacts with plasma proteins in a variety of ways.
- Upon interstitial administration, ICG can be used for optical guidance during lymphatic mapping for SLNB.
- The physicochemical properties of quantum dots and their applications for lymphatic mapping are described in this section.

3.7 Multimodal Tracers for Lymphatic Mapping

The recent development of nanotechnology has enabled to produce new multimodality functional imaging probes. PET/optical dual-functional imaging probes are imaging agents which combine both a PET tracer and fluorescent tracer, allowing the convenient use of the combined system with single injection [158]. Fluorescence and gamma-emitting agents can also be conjugated for preoperative imaging and for intraoperative guidance [149]. In fact, the radionuclide provides deep-tissue imaging of the whole body, while optical imaging enables a longitudinal study even after radionuclide decay. Moreover, optical and PET or SPECT imaging can be cross-validated with dual-function probes, since replacing isotopes with fluorescent markers may affect the biodistribution of a tracer [159]. For example, Evans blue (EB), a dye molecule binding with plasma proteins, has been labeled with ^{99m}Tc (^{99m}Tc-EB, Fig. 3.12) for SLN mapping. ^{99m}Tc-EB combines both radioactive and optical signals and can be administered as a single injection for SLN identification [160]. A hybrid fluorescent-radioactive tracer has also been applied for SLN mapping by mixing ICG with ^{99m}Tc-labeled albumin nanocolloid (Fig. 3.13) [161]. The lymphatic drainage pattern of ICG/^{99m}Tc-nanocolloid is identical to that of ^{99m}Tc-nanocolloid in the clinical setting and all preoperatively identified SLNs could be localized using combined radio- and fluorescence guidance intraoperatively.

Similarly, NIR/MR dual probes for lymphatic imaging have also been developed [162]. With these probes, both NIR and MR imaging can be obtained following a single injection. Most of the PET/MR and SPECT/MR bimodal imaging probes are nanoparticles or nano-sized structures, because it is difficult for small molecules to carry two or more imaging reporters and even targeting groups as a single entity due to their limited loading capacity (Table 3.5). The advantage of nano-sized structures is that they allow for carrying multimodal imaging reporters and targeting biomolecules. Approaches for the development of novel multimodal PET/SPECT-MR probes are mainly through surface modifications, by conjugating an MR imaging reporter such as paramagnetic Gd^{3+} or superparamagnetic iron oxides (SPIOs),
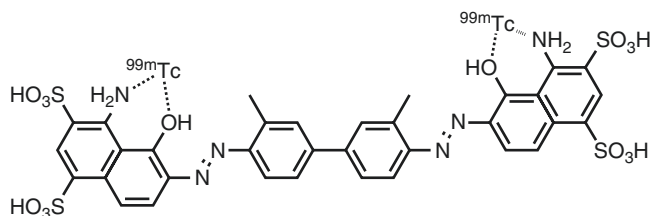

Fig. 3.12 Chemical structure of ^{99m}Tc-labeled Evans blue (^{99m}Tc-EB), with two ^{99m}Tc atoms conjugated with a single EB molecule

Fig. 3.13 Schematic process of ICG conjugation with ^{99m}Tc-albumin nanocolloid. γ denotes radiation emitted from the radionuclide ^{99m}Tc, while λ denotes frequency of lights exciting ICG and, in turn, emitted by ICG (*reproduced with permission from ref* [89]: *Buckle T, van Leeuwen AC, Chin PT, Janssen H, Muller SH, Jonkers J,* et al. *A self-assembled multimodal complex for combined pre- and intraoperative imaging of the SLN. Nanotechnology. 2010;21(35):355101*)
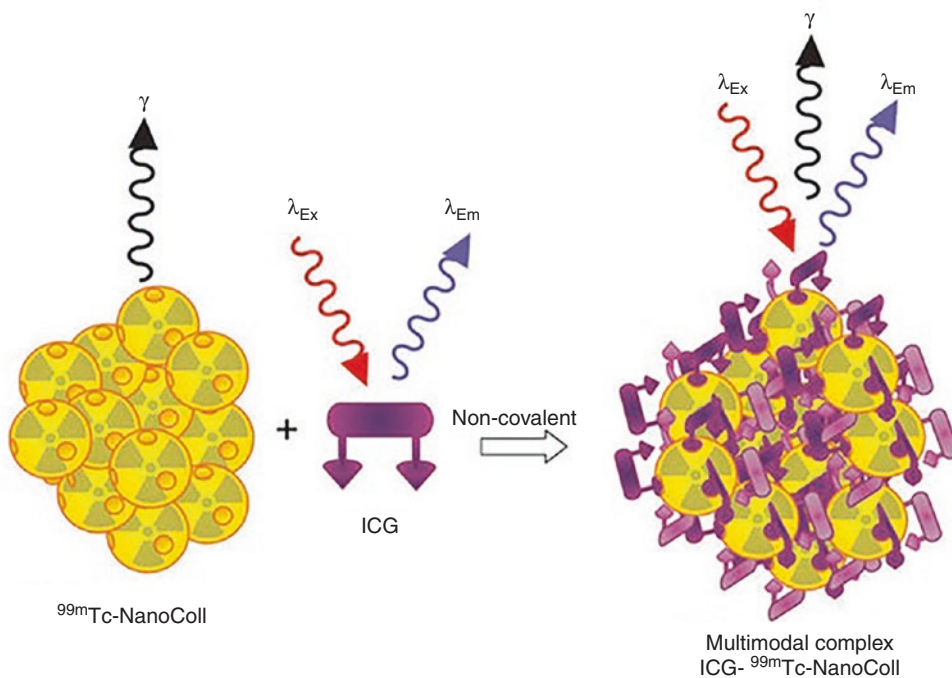

Table 3.5 Bimodal agents for imaging lymph nodes (LNs), including SLN mapping

Probe	PET or SPECT reporter	MR reporter	Applications	References
^{124}I-SA-MnMEIO	^{124}I	MnFe$_2$O4	Axillary and brachial LNs imaging	[163]
^{68}Ga-NOTA-IO-Man	^{68}Ga	SPIO	LN imaging	[164]
^{64}Cu-DTCBP-SPION	^{64}Cu	SPION	LN mapping	[165]
^{99m}Tc-SPIONs	^{99m}Tc	SPION	SLN mapping	[166]
^{69}Ge-SPION	^{69}Ge	SPION	SLN mapping	[167]
^{89}Zr-ferumoxytol	^{89}Zr	Ferumoxytol	SLN mapping	[168]

and by incorporating a PET/SPECT radionuclide together with other functionalities.

SPIOs with a composition of MnFe$_2$O$_4$ (MnMEIO) coated with serum albumin were used to radiolabel the protein with ^{124}I (^{124}I-SA-MnMEIO) as a bimodal imaging probe to image SLNs in vivo [163]. ^{124}I-SA-MnMEIO can be directly radiolabeled by conjugation of ^{124}I with the ortho position of tyrosine residue in albumin using Iodo-Beads. The ^{124}I ion from Iodo-Beads in solution will be oxidized to form a reactive ^{124}ICl species, which reacts with the ortho position of tyrosine. Two different LNs, brachial and axillary LNs, could be clearly identified and localized with PET/MR fusion imaging; however, axillary LN was unambiguously spotted when MRI single modality was used only due to its location far

from the injection site compared with brachial LN. A dual-PET/MR imaging probe, ^{68}Ga-NOTA-IO-MAN, was synthesized using a new methodology for targeting LNs [164]. A different strategy was developed to radiolabel clinically approved SPIOs such as Endorem/Feridex. A bifunctional chelator dithiocarbamate bisphosphonate (DTCBP) was conjugated with Endorem with high affinity for both the metallic radionuclide ^{64}Cu and dextran-coated SPIO nanoparticles to facilitate the radiolabeling in high yields, providing a highly stable bimodal probe both in vitro and in vivo [165]. PET/MR imaging studies confirmed the dual probe's potential for imaging SLN in a non-tumor model. SPIOs radiolabeled with ^{99m}Tc were reported as a dual-SPECT/MR probes feasible for imaging SLNs [166]. Both SPECT and MR images showed the accumulation of ^{99m}Tc-SPIONs in LNs after subcutaneous injection in rats. The high uptake of ^{99m}Tc-SPIONs found in SLN from biodistribution studies indicated that ^{99m}Tc-SPIONs could have future applications in breast cancer and malignant melanoma. Inspired by the technology that the parent ^{68}Ge radionuclide in the ^{68}Ge/^{68}Ga generator is bound to metal oxide TiO$_2$, the SPIONs were labeled with ^{69}Ge in the absence of a chelator, as a PET/MR probe. Incorporating PET radionuclides such as ^{69}Ge and ^{59}Fe into SPIOs without a chelator during the nanoparticle synthesis is one of the new synthetic approaches to generating multimodal nanoparticles. For example, a dual-PET/MR probe ^{69}Ge-SPION@PEG was prepared by incorporating ^{69}Ge, which was generated by ^{69}Ga(p,n)^{69}Ge from a cyclotron, into SPIOs for SLN imaging. The hydrophilic coating poly(acrylic acid) (PAA) of SPION was PEGylated to increase the in vivo stability. Uptake of ^{69}Ge-SPION@PEG

Table 3.6 Trimodal agents for imaging lymph nodes (LNs), including SLNs

Probe	PET (SPECT) reporter	MR reporter	Third imaging reporter	Applications	References
[124]I-TCL-SPIONs	[124]I	SPION	[124]I Cherenkov radiation as optical	SLN imaging	[169]
^{68}Ga-SPION	[68]Ga	SPION	[68]Ga Cherenkov optical	SLN imaging	[170]
[68]Ga[MNPSiO2(NIR797)]	[68]Ga	CoFe2O4	NIR797 fluorescence	SLN imaging	[171]
[64]Cu-DOTA-MSN-Gd-DTTA-FTIC	[64]Cu	Gd-DTTA	FTIC fluorescence	SLN mapping and tumor metastases	[172]
[64]Cu-ZW800-Gd3-MSN	[64]Cu	Gd3-MSN	ZW800 fluorescence	SLNs	[173]

in normal BALB/c mice in the popliteal LN from in vivo PET images and contrast enhancement in MR images demonstrated its possible application in LN mapping [167].

Another PET/MRI multimodal nanoparticle, ^{89}Zr-ferumoxytol, has been tested in preclinical disease models, the results demonstrating that the particles can be used for high-resolution tomographic studies of lymphatic drainage [168].

Even more complex, trimodal imaging has emerged as a novel imaging strategy for translational research, which combines three different modalities together such as PET/SPECT-MR-Optical to provide complementary information and achieve synergistic advantages over any single modality alone (Table 3.6). The main challenge of trimodal imaging lies in developing an efficient platform that incorporates various imaging modality reporters without disturbing each other while maintaining the entity intact.

A very interesting approach for the preparation of a PET/MR/optical trimodal imaging probe is based on ^{124}I conjugation with SPIO nanoparticles. Clearly, the trimodal nanoparticles are characterized by the long physical emission half-life of ^{124}I (4.2 days). Their emission of high-energy positron decay with a β^+ mean energy of 819 keV led to strong Cherenkov radiation as an optical imaging reporter in which no fluorescent dye is needed, unlike in the case of previously described trimodal imaging reporter probes. SPION with cross-linked polymer coating layers containing PEG (TCL-SPION) was selected as an MR imaging reporter [169]. Consistent results were also found in the ex vivo optical and micro-PET images of the dissected LNs. Similar to ^{124}I, ^{68}Ga enables Cherenkov radiation that can be used as an optical imaging reporter [170] MNP-SiO$_2$(NIR797), a magnetic silica nanoparticle encapsulating the NIRF dye in a silica shell, was reported as a trimodal PET-MR-NIRF probe for in vivo SLN imaging in mice. Nanoparticles with particle size of 45 ± 6 nm were selected for SLN mapping, as they were optimal for entering the lymphatic vessels and retaining in the capillary vessels within the lymphatics. The trimodal tracer was injected into the forepaw of mice for SLN mapping using PET, MR, and NIRF. When 100 µg of ^{68}Ga-MNPSiO$_2$(NIR797) was subcutaneously injected, PET images of axillary and brachial LNs and clear signals of NIRF in axillary and brachial

LNs could be obtained; however, MR imaging of axillary LNs was possible only at doses higher than 200 µg of ^{68}Ga-MNPSiO$_2$(NIR797) [171]. When radiolabeling with [^{18}F]fluoride or ^{64}Cu/^{99m}Tc-bisphosphonate (BP) conjugates to Fe$_3$O$_4$@NaYF4 core/shell nanoparticles with different cation dopants in the shell or core, the inorganic core-shell nanoparticles were applied as trimodal probes for SLN imaging. In vivo LN imaging studies showed obvious advantages of combining different imaging modalities. When combined with highly sensitive PET, but not MRI alone, the in vivo imaging studies offered improved presurgical mapping of iliac and popliteal LN locations and provided more details to interpret SLN imaging that are relevant to the pathology of LNs and tumor metastasis in humans. Fluorescence could offer additional information of anatomical and functional changes during surgery and subsequently during pathological examination of excised tissues [172]. A mesoporous silica-based triple-modal imaging nanoprobe (MSN-probe) possesses the long-term imaging ability to track tumor metastatic SLNs. In this system, three imaging tags including the NIR dye ZW800, T1 contrast agent Gd^{3+}, and positron-emitting radionuclide ^{64}Cu were integrated into MSNs by different conjugation strategies. Due to their high stability and long intracellular retention time, signals from tumor draining SLNs are detectable up to 3 weeks. These examples demonstrate the advantages of using a PET/SPECT-MR bimodal probe for SLN mapping, which can be used to further evaluate the metastatic status of a tumor [173].

Key Learning Points

- Hybrid multimodal agents include ^{99m}Tc-Evans blue, ICG conjugated with ^{99m}Tc-albumin nanocolloid, Gd^{3+}, or superparamagnetic iron oxides (SPIOs) by incorporating a PET/SPECT radionuclide with its associated functionalities, such as ^{124}I-SA-MnMEIO, ^{68}Ga-NOTA-IO-MAN, ^{99m}Tc-SPIONs, ^{69}Ge-SPION@PEG, ^{89}Zr-ferumoxytol, MNP-SiO2(NIR797), ^{68}Ga-MNPSiO2(NIR797), and ^{64}Cu- or ^{99m}Tc-bisphosphonate conjugates to Fe3O4@NaYF4 core/shell nanoparticles.

3.8   Instrumentations for Lymphatic Mapping

Conventional SLN mapping is based on the combined use of blue dye and lymphoscintigraphy, or on lymphoscintigraphy alone, with the perspective of using PET/CT or PET/MR imaging sometimes in the future [174]. To increase the performance of the SLN procedure over conventional imaging with large field-of-view gamma cameras, intraoperative portable gamma cameras have recently been developed to obtain preoperative imaging of the SLN. The following sections provide a review of the available intraoperative probes and portable imaging devices, their working principle, and clinical implementation.

3.8.1   Intraoperative Probes for Radioguided Surgery

The working principle of the intraoperative probes for SLN detection (also called gamma probes) is the conversion of the 140 keV photons emitted by ^{99m}Tc into electrons by photoelectric effect or Compton scattering and the production of a signal processed by a custom readout electronics [175]. Indeed, most commercially available handheld gamma detection probes are generally designed for detecting radioisotopes of gamma-ray energies in the low-energy emission range (up to 150 keV) and medium-energy emission range (150–400 keV), which enable to detect radioisotopes such as ^{99m}Tc (140 keV), ^{111}In (171 keV and 247 keV), ^{123}I (159 keV), and ^{125}I (35 keV).

The intraoperative probes for SLN detection can be divided into two main categories: the first one includes probes based on scintillation detectors (both crystal and plastic types), while the second group includes the semiconductor-based probes [176–184]. The typical configuration for intraoperative probes, both for scintillator or semiconductor, is shown in Fig. 3.14.
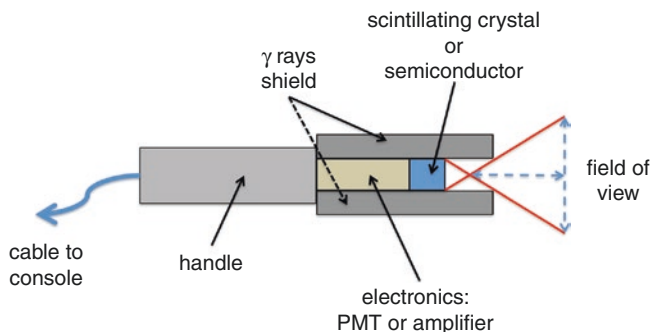

Fig. 3.14 General design of a handheld intraoperative gamma probe for intraoperative search of the target tissue (SLN or tumor) to be resected during surgery, with schematic representation of its main components

The most significant parameters defining the performances of gamma probes are (1) overall sensitivity (efficiency), (2) spatial resolution (radial and lateral), (3) energy resolution, and (4) signal-to-noise ratio.

Sensitivity is the detected count rate per unit of activity and it is determined at the tip of the probe. Radial resolution is the width of the measurement cone where the radiation is detected at a defined distance. With a wider cone, background signal may overcome the signal generated at the target source. With a narrower cone, background is reduced and detection of the target source is more accurate. Lateral spatial resolution is the capability to accurately localize the position of a target source and to separate two adjacent sources. Energy resolution is the capacity of the gamma detection system to discriminate between radiations of different energies. This property is essential to distinguish between two simultaneously administered radionuclides that have different energies and to discriminate scattered from primary photons. The latter property relates to the ability of the probe to discriminate the signal from the target with respect to the noise represented by the background radiation within the surrounding tissue.

The scintillator absorbs the radiation and emits a number of visible photons proportional to the energy absorbed; in turn, visible light is measured by using a photon detector, usually a photomultiplier (PMT). The crystals used for scintillator detector probes include thallium-activated sodium iodide (NaI[Tl]), thallium-activated cesium iodide (CsI[Tl]), cerium-activated lutetium orthosilicate (LSO[Ce]), bismuth germanate (BGO), and cerium-doped gadolinium orthosilicate (GSO[Ce]).

The high penetration power of gamma rays means that background events could come from parts of the patient outside the target volume of interest. Although a fraction of these events is attenuated within the patient body, in order to further reduce the background the gamma probes are equipped with a shield (material such as lead, tungsten, gold, or platinum), and collimators (designed with different lengths and apertures for different field of views, FOV) that prevent attenuated radiation from nontarget locations (i.e., scattered radiation) from accessing the detector head and thus producing spurious counts. Side- and back-shielding can be important when there is a localized radiation source (the injection site of the ^{99m}Tc-labeled agent for radioguided SLNB) in close proximity with the target (the SLN). Collimation of the detector head results in better spatial resolution and higher signal-to-noise ratio as compared to radiation emitted from surrounding tissues. However, when collimation is too pronounced it reduces sensitivity of the probes, by decreasing the detection aperture and lengthening the distance to the actual source position. Furthermore, a thicker shielding or a longer collimator is needed when detecting higher energy gammas, but this increases the overall weight and size of the gamma probe.

The final elements in the system are the electronics and the readout. Since the scintillator detector provides a signal proportional to the deposited energy, it is possible to make spectroscopy and to set the sensitive energy range of the probe to select the desired gamma energy and eliminate part of the scattered radiation. The count rate of the probe is then fed to a ratemeter, which also drives an audio output. An increase in loudness or frequency indicates to the surgeon proximity of the probe to the target tissue.

Semiconductors are a valid alternative to scintillators as detector material for the intraoperative probes. When radiation is absorbed in a solid-state detector, ionization occurs by promoting electrons out of the valence band to the conduction band where electrons can flow in the crystal lattice. When the electron moves to the conduction band, a positive charge (hole) in the lattice is created which is free to move in the valence band. If an electric field is applied across the sensitive volume of the detector, the excess of charge (both electrons and holes) is collected by the opposite electrodes, thus providing a signal which is proportional to the energy released in the detector. Crystalline materials that are used in such detectors are cadmium telluride (CdTe), cadmium zinc telluride (CdZnTe), and mercuric iodide (HgI_2).

Scintillation-based detection systems present both pros and cons with respect to semiconductor-based systems. On the one hand, scintillator-based detectors have a higher sensitivity (because of the higher density and atomic number they are better suited for medium-to-high gamma energy detection), but a poorer energy resolution and scatter rejection due to the indirect mechanism of the radiation detection (the primary gamma converts in the scintillator, then the light should be conveyed to the PMT, and the signal finally converted from optical to electrical). Furthermore, scintillation-based detectors tend to have a much bulkier probe head profile and weight. On the other hand, semiconductor-based probes are direct detectors (the energy released in the material by radiation is directly converted into a charge signal) and thus they have a higher energy resolution and scatter rejection capability. Likewise, semiconductor-based probes tend to have a much more compact probe head design; they can be manufactured in small size and they can have a very thin entrance window that enables to count low-energy beta and gamma rays.

To improve SLN localization using a gamma probe during surgery, a novel technological possibility is the so-called freehand SPECT device that combines a positioning system attached to the conventional gamma probe with a tracking system on the patient's body and permits virtual reconstruction of the position of a radioactive source in a 3-D environment. In particular, the system combines acoustic signals with 3-D imaging for the localization of areas with focal radioactivity accumulation in the operating room. The system consists of a spatial localization system and two tracking targets that are fixed on the gamma probe and on the patient,

respectively [185]. The localization system consists of an optical camera and an infrared localization device. The 3-D images generated with the freehand SPECT probe are visualized on the screen. The images can be displayed in real time so that information on the depth of a lymph node (or of other radiolabeled target tissue of interest, e.g., a hyperfunctioning parathyroid adenoma upon administration of ^{99m}Tc-sestamibi) is available (Fig. 3.15).

After the development of PET lymphoscintigraphy techniques (described in Chap. 4), handheld gamma detection probes specifically designed for detecting the high-energy 511 keV photon emissions generated by the electron-positron annihilation process, characteristic of radionuclides such as ^{18}F or ^{68}Ga, have recently become available. These probes have been designated as "PET" probes. The overall weight and size of these probes are generally dependent on the thickness of side- and back-shielding (typically in lead, tungsten, gold, or platinum) and the length of the collimator [186]. To improve the current "PET" probe design (increase of side/back-shielding, or collimation length, or crystal diameter/thickness) without resulting in configurations that are too large in size, too heavy, and of greater cost, novel "PET" probe designs are being developed in which the efficacy is not dependent upon side- and back-shielding, collimation, or crystal diameter/thickness. Examples of such probes are secondary K-alpha X-ray fluorescence [187, 188], active electronic collimation [188], and other crystal geometry designs using multiple small crystals with specific novel geometric configurations for optimizing and maximizing background rejection capabilities [188].

Many commercial intraoperative gamma probes are available; an example of a gamma probe with its console (control unit) is presented in Fig. 3.16 [189].

Several factors determine the choice of a particular intraoperative probe. From the point of view of the surgeon, there are many desirable design features of detection probe systems that are important [175, 182]. Gamma probes for radioguided SLNB require high spatial resolution to allow for a more precise localization of small lymph nodes.

Other features such as the shape, weight, and ergonomical design of an intraoperative probe are critical. The audible signal and digital display of the detector control unit are also important for providing critical output information to the surgeon, enabling quick and accurate localization of the radionuclide without distraction from the overall activity in the surgical field. Flexibility and adaptability of the system are also functional to different clinical issues, such as removable side-shielding, interchangeable collimators, interchangeable detector probes, and user-adjustable energy windows for different radionuclides. Finally, the recent development of handheld self-contained gamma detection probes based on wireless Bluetooth technology eliminates the need for cables that normally connect the probe to the control unit [190, 191].
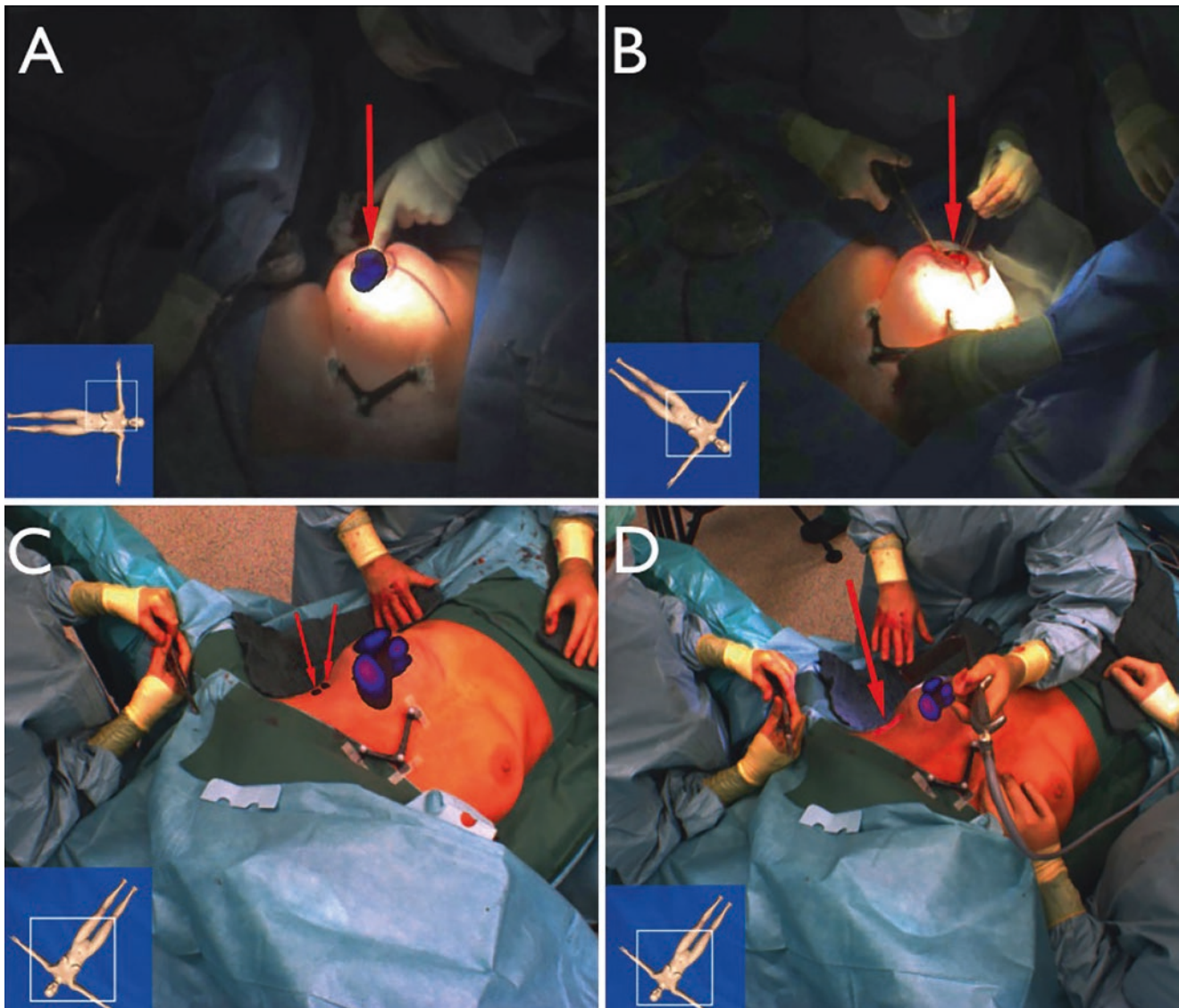
Fig. 3.15 Freehand SPECT device used for radioguided surgery in a patient with non-palpable breast cancer. (**a**) Overlay of freehand SPECT 3-D image on the video display shows high retention of radiocolloid at the intratumoral injection site. (**b**) After tumor removal, the absence of radioactivity accumulation in the surgical field confirms complete excision of the tumor. (**c**, **d**) A similar approach is used to guide the surgeon for complete removal of SLNs (red arrows) (*reproduced with permission from ref* [185])

Key Learning Points
- Main kinds of handheld gamma probes for intraoperative use during radioguided surgery have been developed, depending on specific clinical use.
- Gamma probes for SLN detection can be divided into two categories: probes based on scintillation detectors (both crystal and plastic types) and probes based on semiconductor detectors.
- The physical principles most commonly used in gamma probes are the scintillation in an organic or inorganic material, and the production of electron-hole pairs in a semiconductor.
- Different materials are used for either scintillation or semiconductor gamma probes.
- Compact, ergonomical, flexible gamma probes for radioguided biopsy of the SLN with high spatial resolution have been developed.

Fig. 3.16 Commercial gamma probe (upper left panel), with diagram of the detector's structure (right panel), and control unit (lower left panel)
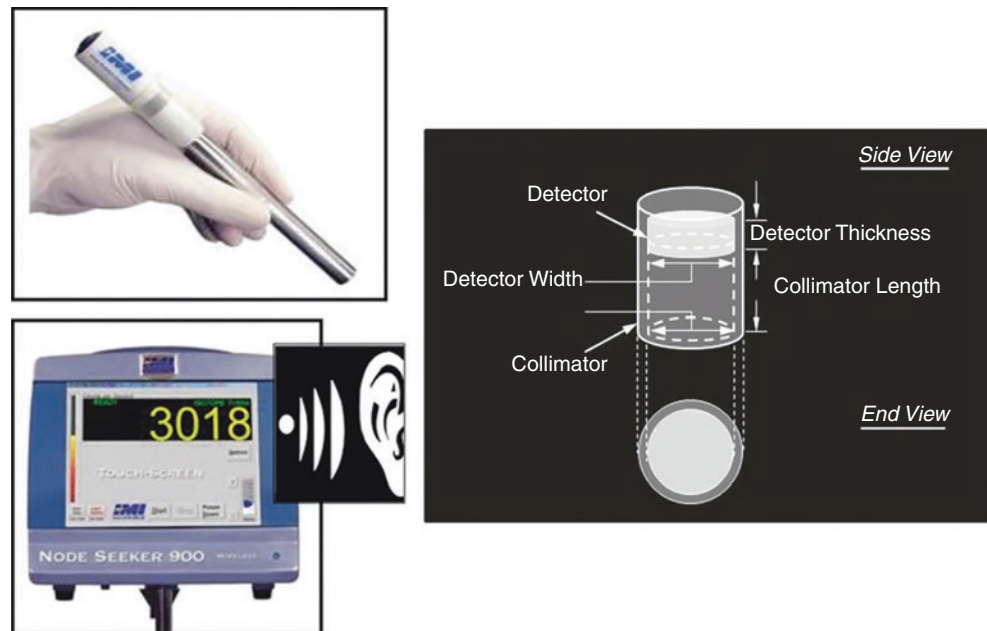
3.8.2 Portable Gamma Cameras for Lymphatic Mapping

Although non-imaging intraoperative probes are still the standard equipment for detection of the radiolabeled tissue in the operating room, they cannot provide further details on source configuration. The exact localization of a source can only be performed if the tip is under direct contact with the tissue after the surgical incision.

In this regard, intraoperative real-time imaging with portable gamma cameras provides an overview of all radioactive hot spots in the whole surgical field [180, 192]. For instance, its position can be adjusted to also show SLNs near the injection area, which can easily be overlooked by using the non-imaging probe. Discriminating a SLN from an upper-tier node is based on the amount of counts simultaneously recorded with the camera, which can be correlated to the preoperative scintigraphic images. The gamma camera can also be used in conjunction with the gamma probes.

Imaging devices must meet several requirements to be employed for the intraoperative use. Among them are a portable and stable design, no delay between image acquisition and display (real-time imaging), and possibility for continuous monitoring, spatial orientation on screen, real-time quantification, and display of the counts recorded. Finally, they should also have an adequate spatial resolution, sensitivity, and field of view.

Examples of such cameras are shown in Fig. 3.17. While the first devices were quite heavy and bulky handheld devices, new-generation portable gamma cameras are lighter and/or equipped with stable support systems.

Among the instruments available on the market, we mention only few that implement these requirements with different approaches in the radiation detector. One of the most widely used devices is the Sentinella S102 (from Oncovision, Valencia, Spain) [193] that is equipped with a CsI(NA) continuous scintillating crystal readout by PSPMTs and different collimators (pinhole collimators, 2.5 and 4 mm in diameters, and divergent) (Fig. 3.17a). The pinhole collimator enables visualization of the whole surgical filed depending on the distance between the camera and the source. The field of view is 4×4 cm at 3 cm from the source, and 20×20 cm at 15 cm from the source. This device has been integrated in a mobile and ergonomic support that is easily adjustable. The imaging head is located on one arm that allows positioning on the specific area. Another approach is based on the use of the CZT as radiation detector. For instance in the Anzai eZ-SCOPE Handheld Gamma Camera [194], the detector is made of a single tile of CdZnTe, patterned in an array of 16×16 pixels at a pitch of 2 mm. The head is equipped with a series on interchangeable parallel-hole collimators to achieve different performances in terms of spatial resolution and/or sensitivity. The field of view is 3.2×3.2 cm and weight is 800 g (Fig. 3.17b).

A further development of the intraoperative gamma camera is the LumaGEM from Gamma Medica Ideas [195]. It is based on the CZT pixel technology and was originally developed for breast gamma imaging. The field of view is 13×13 cm and the intrinsic spatial resolution is 2 mm. This camera is also equipped with exchangeable parallel hole collimator and it is integrated in a work-stand articulated arm.

Recent technological advances lead to speculate that, in the near future, the PMT-based systems will be

Fig. 3.17 Examples of portable gamma cameras for intraoperative use: (**a**) Recent-generation portable gamma camera with improved ergonomical details and adequate support system for intraoperative use (model Sentinella S102, manufactured by Oncovision, Valencia, Spain). (**b**) Portable gamma camera with a weight <1 kg but without support system (eZ-Scope, manufactured by Anzai Medical, Tokyo, Japan)

replaced with cameras based on scintillators coupled with solid-state photodetectors. In these systems the photodetector will be an array of photodiodes (more likely silicon photomultipliers, the so-called SiPM) coupled to a slab or a matrix of crystals designed to be coupled one to one to the photosensors [196]. In such a way, the thickness of the detector (including crystal, photodiodes, and electronics) coupled to a shallow collimator could be less than 5 cm, so that it would be compact enough to be brought into a surgery room as an intraoperative imaging probe.

Most beta probes commercially available are nonimaging systems and therefore suffer from the lack of ancillary information of the tissue area to be explored. A novel, handheld digital imaging beta probe (IBP), suitable for use during surgery in conjunction with beta-emitting radiopharmaceuticals such as [^{18}F]FDG, for real-time imaging of a surveyed area with higher spatial resolution and sensitivity, lower sensitivity to background radiation, and greater ease of operation than existing instruments, is shown in Fig. 3.18 [197]. This is a visual mapping device to locate and confirm excision of [^{18}F]FDG-avid primary tumors and metastases. The proposed handheld IBP includes a 140 μm thick microstructured CsI:Tl film optically coupled to a highly sensitive electron-multiplying charge-coupled device (EMCCD) via a flexible fiber-optic (FO) conduit. The microcolumnar structure of the CsI:Tl scintillator minimizes the spread of scintillation light to typically less than 100 μm, and allows for the detection of beta radiation with high spatial resolution. The EMCCD is a back-thinned, thermoelectrically cooled (−35 °C), 512 × 512-pixel CCD optically bonded to a 1:1 fiber-optic (FO) window. The EMCCD has 16 × 16 μm pixels, and an effective imaging area of approximately 8.2 × 8.2 mm. The

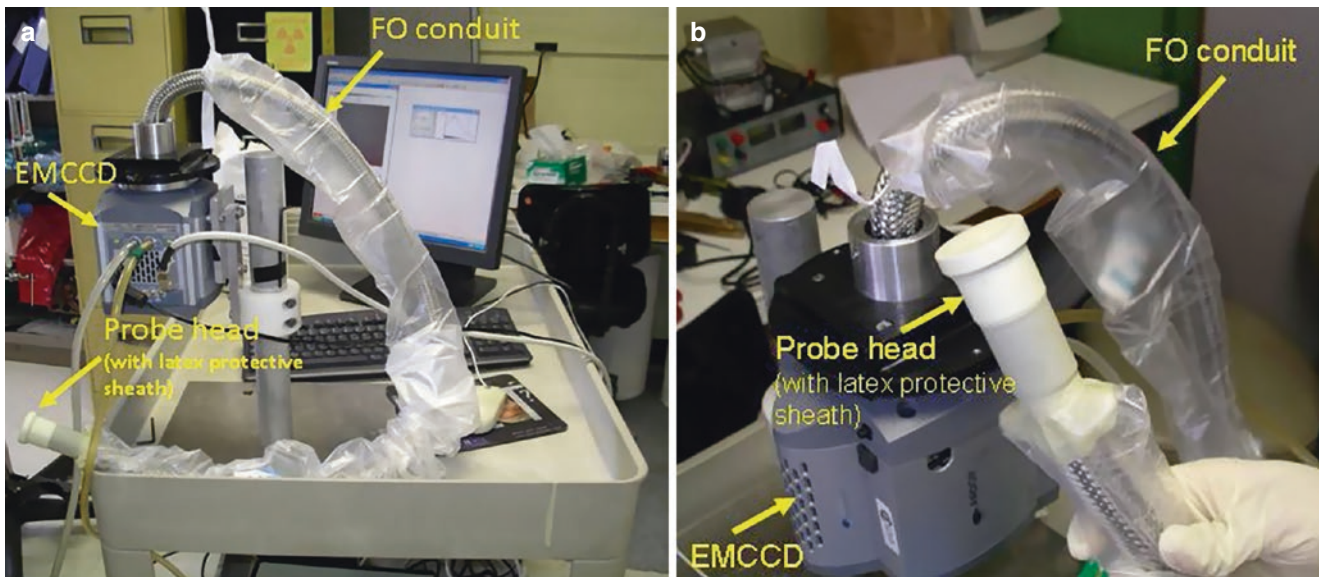
Fig. 3.18 (a) Prototype of the handheld Imaging Beta Probe™ (IBP™). (b) Close-up view of the probe head, covered by a latex sheath (*reproduced with permission from ref.* [197])

advantage of the EMCCD is that it internally amplifies the signal with a user-selectable gain and minimizes the noise associated with the CCD readout amplifier by the same gain factor. In order to increase its active imaging area, a 2:1 or 3:1 FO taper is coupled to the IBP's FO conduit, resulting in an effective imaging area of 16.4×16.4 mm or 24.6×24.6 mm, respectively. An index matching fluid is used for the optical coupling of each of the three interfaces between the FO faceplate, 3:1 FO taper, FO bundle, and EMCCD. A 24 µm thick aluminum foil (negligible attenuation of β-radiation) is placed in front of a CsI(Tl) film to shield the IBP from ambient light. Due to its high density and high average atomic number the CsI:Tl film, while only ~140 µm thick, completely absorbed and enabled the detection of every incident beta particle, while being highly insensitive to gamma background. Furthermore, the high light output of CsI(Tl) (56,000 ph/MeV) and high sensitivity of the EMCCD photodetector increased overall IBP sensitivity and effectiveness.

Key Learning Points
- Handheld gamma probes for radioguided surgery have been developed for a wide variety of applications and are commercially available.
- With the development of PET lymphoscintigraphy techniques, dedicated "PET" probes specifically designed for detecting resultant high-energy 511 keV gamma emissions have become available.

3.9 Near-Infrared (NIR) Imaging for Lymphatic Mapping

An impressive surge of interest has recently occurred for fluorescence-guided surgery, which has led to a steady demand for new commercial fluorescence imaging devices. For the greatest clinical impact, an imaging system must provide a solution to the immediate clinical goal with important new information that affects the patient outcome in a way that seamlessly blends into current clinical workflow. There are several new fluorescence imagers that have been cleared for commercial use by the 510(k) process at the U.S. FDA for open-surgical use with ICG (Table 3.6) [198].

Near-infrared (NIR) imaging using for example ICG has been developed for functional imaging of location and patency of vascular structures in neuro-, ophthalmologic, and vascular surgeries since the 1980s. The wavelength of NIR light is approximately 700–1000 nm. This range is the least absorbed by blood or water; thus, this "optical window" has been regarded as the best wavelength of imaging to provide the deepest penetration of the signal. Subsequently, ICG NIR imaging has been applied to various procedures in general surgery, providing functional information of the perfusion of the organs, visualization of the biliary tract and hepatic tumors, and margins of the anatomic segments of the liver. NIR imaging systems are composed of excitation light sources and special filters and cameras optimized for the NIR wavelength of light. ICG is excited at 700–800 nm, and the emitted maximal signal is 800–840 nm [199, 200]. For ICG fluorescent imaging (FI), the fluorescent dye ICG is intravenously administered through a peripheral venous line

and the tissue in the region of interest is illuminated with near-infrared light at a wavelength of 785 nm with a total output of 80 mW in a field of view of 10 cm in diameter (1 mW/cm^2) operating at a distance of approximately 20 cm above the tissue. The fluorescence emission of the excited dye is detected by an infrared-sensitive charge-coupled device (CCD) camera system. The camera is equipped with a band-pass filter for the selective transmission of light at the emission maximum of ICG (830 nm) (Fig. 3.19). The fluorescent imaging images are then displayed and recorded in real time on a computer monitor. The laser has an excellent safety profile for both patient and operating staff. Because of the low power density of the emitted laser energy, there is no tissue warming. Although ICG-FI has turned to be a more and more common technique to evaluate intraoperative organ perfusion, only few studies tried to quantitatively validate the technique for visceral perfusion assessment [201].

Figure 3.20 and Table 3.7 summarize the current leading fluorescence guidance systems. The PerkinElmer Solaris, Curadel ResVet LabFlare, and SurgVision Explorer Air are not 510(k) cleared for human use, while the others are for ICG procedures. All of them can image ICG in surgical trials, with differing levels of sensitivity and with different features [198].
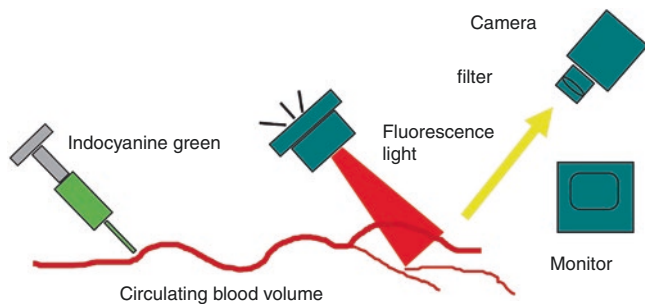

Fig. 3.19 Indocyanine green fluorescent imaging (IDG-FI): After intravenous injection, the region of interest is illuminated with near-infrared light (785 nm). The fluorescence emission of the excited dye is detected by an infrared-sensitive charge-coupled device camera system (dynamic range 54 dB) equipped with a band-pass filter for the selective transmission of light at the emission maximum of ICG (830 nm) (*reproduced with permission from ref.* [201])

> **Key Learning Points**
> - With the recent development of fluorescence-guided surgery, new fluorescence imaging devices have become commercially available.
> - Among near-infrared techniques, indocyanine green fluorescence is the most commonly used for functional imaging of vascular structures in neuro-, ophthalmologic, and vascular surgeries.

PerkinElmer Solaris   Novadaq SPY-Elite   Quest Spectrum   Curadel ResVet LAB-Flare   Visionsense Iridium   SurgVision prototype

Fig. 3.20 Current leading fluorescence-based guidance systems. From left to right: Solaris™ Open-Air Fluorescence Imaging System (printed with permission, 2015–2016 PerkinElmer, Inc., all rights reserved); NOVADAQ Spy-Elite™ (copyright 2016 Novadaq Technologies Inc.); Quest Spectrum™ (copyright Quest Medical Imaging); Fluobeam®, Hamamatsu PDE-Neo™ (copyright 2016 Fluoptics); Lab-FLARE® Model R1 (copyright CURADEL); Visionsense Iridium™ (copyright Visionsense); SurgVision Explorer Air prototype (image courtesy of SurgVision) (*reproduced with permission from ref.* [24]*: DSouza AV, Lin H, Henderson ER, Samkoe KS, Pogue BW. Review of fluorescence guided surgery systems: identification of key performance capabilities beyond indocyanine green imaging. J Biomed Opt. 2016;21(8):80901*)

Table 3.7 ICG fluorescence imaging systems approved through FDA clearance based on the 510(k) process, after demonstration of the device being safe and effective, with substantial equivalence to a predicate device [198]

Company	Fluorescence imaging system	Year approved/510(k) cleared	FDA 510(k) number	Indication approved for
Novadaq Technologies, Inc.	SPY imaging system	2005	K042961	Blood flow
Novadaq Technologies, Inc.	SPY imaging system SP2000	2007	K063345	Tissue perfusion and transfer circulation in free flaps, plastic, and reconstructive surgery
Novadaq Technologies, Inc.	SPY fluorescent imaging system SP2001	2008	K073088	510(k) with SPY SP2000
Novadaq Technologies, Inc.	SPY fluorescent imaging system SP2001	2008	K073130	510(k) for modified device
Novadaq Technologies, Inc.	SPY intraoperative imaging system	2011	K100371	Additional gastrointestinal imaging
Hamamatsu Photonics K.K.	PDE photodynamic eye	2012	K110480	510(k) with SPY K063345 and K073130
Hamamatsu Photonics K.K.	PDE Neo	2014	K133719	510(k) with PDE K110480 for modified device
Fluoptics	Fluobeam 800 clinical imaging device	2014	K132475	510(k) with PDE
Quest Medical Imaging	Artemis light engine	2015	K141164	510(k) with Karl Storz and Olympus Winter
Quest Medical	Artemis handheld imaging system	2015	K143474	510(k) with PDE and Fluobeam 800
VisionSense Ltd.	VS3-IR-MMS system	2015	K150018	510(k) with SPY 063345

References

1. Walker LA. Localization of radioactive colloids in lymph nodes. J Lab Clin Med. 1950;36:440–9.
2. Segal AW, Gregoriadis G, Black CD. Liposomes as vehicles for the local release of drugs. Clin Sci Mol Med. 1975;49:99–106.
3. Ikeda I, Inoue O, Kurata K. New preparation method for ^{99m}Tc-phytate. J Nucl Med. 1976;17:389–93.
4. Strand SE, Persson BR. Quantitative lymphoscintigraphy I: basic concepts for optimal uptake of radiocolloids in the parasternal lymph nodes of rabbits. J Nucl Med. 1979;20:1038–46.
5. Bergqvist L, Strand SE, Persson BR. Particle sizing and biokinetics of interstitial lymphoscintigraphic agents. Semin Nucl Med. 1983;13:9–19.
6. Turner JH. Post-traumatic avascular necrosis of the femoral head predicted by preoperative technetium-99m antimony-colloid scan. An experimental and clinical study. J Bone Joint Surg Am. 1983;65:786–96.
7. Patel HM, Boodle KM, Vaughan-Jones R. Assessment of the potential uses of liposomes for lymphoscintigraphy and lymphatic drug delivery. Failure of 99m-technetium marker to represent intact liposomes in lymph nodes. Biochim Biophys Acta. 1984;801:76–86.
8. Patel HM, Russell NJ. Liposomes: from membrane model to therapeutic applications. Biochem Soc Trans. 1988;16:909–10.
9. Strand SE, Bergqvist L. Radiolabeled colloids and macromolecules in the lymphatic system. Crit Rev Ther Drug Carrier Syst. 1989;6:211–38.
10. Allen TM, Hansen CB, Guo LS. Subcutaneous administration of liposomes: a comparison with the intravenous and intraperitoneal routes of injection. Biochim Biophys Acta. 1993;1150:9–16.
11. Moghimi SM, Davis SS. Innovations in avoiding particle clearance from blood by Kupffer cells: cause for reflection. Crit Rev Ther Drug Carrier Syst. 1994;11:31–59.
12. Moghimi SM, Rajabi-Siahboomi R. Advanced colloid-based systems for efficient delivery of drugs and diagnostic agents to the lymphatic tissues. Prog Biophys Mol Biol. 1996;65:221–49.
13. Ikomi F, Hanna GK, Schmid-Schönbein GW. Mechanism of colloidal particle uptake into the lymphatic system: basic study with percutaneous lymphography. Radiology. 1995;196:107–13.
14. Sherman AI, Ter-Pogossian M. Lymph-node concentration of radioactive colloidal gold following interstitial injection. Cancer. 1953;6:1238–40.
15. Pecking A, Firmin F, Rain JD, et al. Lymphoedema of the upper limb following surgery or radiotherapy. Investigation by indirect radioactive lymphography. Nouv Press Med. 1980;9:3349–51.
16. Bräutigam P, Vanscheidt W, Földi E, et al. The importance of the subfascial lymphatics in the diagnosis of lower limb edema: investigations with semiquantitative lymphoscintigraphy. Angiology. 1993;44:464–70.
17. Mostbeck A, Partsch H. Isotope lymphography—possibilities and limits in evaluation of lymph transport. Wien Med Wochenschr. 1999;149:87–91.
18. Partsch H. Practical aspects of indirect lymphography and lymphoscintigraphy. Lymphat Res Biol. 2003;1:71–3; discussion 3–4.
19. Henze E, Schelbert HR, Collins JD, et al. Lymphoscintigraphy with Tc-99m-labeled dextran. J Nucl Med. 1982;23:923–9.
20. Kazem I, Antoniades J, Brady LW, et al. Clinical evaluation of lymph node scanning utilizing colloidal gold 198. Radiology. 1968;90:905–11.
21. Nagai K, Ito Y, Otsuka N, et al. Clinical usefullness on accumulation of ^{99m}Tc-rhenium colloid in lymph nodes. Radioisotopes. 1980;29:549–51.
22. Nagai K, Ito Y, Otsuka N, et al. Deposition of small ^{99m}Tc-labelled colloids in bone marrow and lymph nodes. Eur J Nucl Med. 1982;7:66–70.
23. Warbick A, Ege GN, Henkelman RM, et al. An evaluation of radiocolloid sizing techniques. J Nucl Med. 1977;18:827–34.

24. Davis MA, Jones AG, Trindade H. A rapid and accurate method for sizing radiocolloids. J Nucl Med. 1974;15:923–8.

25. Hung JC, Wiseman GA, Wahner HW, et al. Filtered technetium-99m-sulfur colloid evaluated for lymphoscintigraphy. J Nucl Med. 1995;36:1895–901.

26. Kleinhans E, Baumeister RG, Hahn D, et al. Evaluation of transport kinetics in lymphoscintigraphy: follow-up study in patients with transplanted lymphatic vessels. Eur J Nucl Med. 1985;10:349–52.

27. Gommans GM, Gommans E, van der Zant FM, et al. ^{99m}Tc Nanocoll: a radiopharmaceutical for sentinel node localisation in breast cancer—in vitro and in vivo results. Appl Radiat Isot. 2009;67:1550–8.

28. Swartz MA. The physiology of the lymphatic system. Adv Drug Deliv Rev. 2001;50:3–20.

29. Atkins HL, Hauser W, Richards P. Visualization of mediastinal lymph nodes after intraperitoneal administration of ^{99m}Tc-sulfur colloid. Nucl Med (Stuttg). 1970;9:275–8.

30. Frier M, Griffiths P, Ramsey A. The physical and chemical characteristics of sulphur colloids. Eur J Nucl Med. 1981;6:255–60.

31. Ikomi F, Hanna GK, Schmid-Schönbein GW. Size- and surface-dependent uptake of colloid particles into the lymphatic system. Lymphology. 1999;32:90–102.

32. Aukland K, Reed RK. Interstitial-lymphatic mechanisms in the control of extracellular fluid volume. Physiol Rev. 1993;73:1–78.

33. Swartz MA, Fleury ME. Interstitial flow and its effects in soft tissues. Annu Rev Biomed Eng. 2007;9:229–56.

34. Mariani G, Moresco L, Viale G, et al. Radioguided sentinel lymph node biopsy in breast cancer surgery. J Nucl Med. 2001;42:1198–215.

35. Weiss M, Gildehaus FJ, Brinkbäumer K, et al. Lymph kinetics with technetium-99m labeled radiopharmaceuticals. Animal studies. Nuklearmedizin. 2005;44:156–65.

36. Reddy ST, Berk DA, Jain RK, et al. A sensitive in vivo model for quantifying interstitial convective transport of injected macromolecules and nanoparticles. J Appl Physiol (1985). 2006;101: 1162–9.

37. Mangat S, Patel HM. Lymph node localization of non-specific antibody-coated liposomes. Life Sci. 1985;36:1917–25.

38. Szuba A, Shin WS, Strauss HW, et al. The third circulation: radionuclide lymphoscintigraphy in the evaluation of lymphedema. J Nucl Med. 2003;44:43–57.

39. Paganelli G, De Cicco C, Cremonesi M, et al. Optimized sentinel node scintigraphy in breast cancer. Q J Nucl Med. 1998;42:49–53.

40. De Cicco C, Cremonesi M, Luini A, et al. Lymphoscintigraphy and radioguided biopsy of the sentinel axillary node in breast cancer. J Nucl Med. 1998;39:2080–4.

41. Wilhelm AJ, Mijnhout GS, Franssen EJ. Radiopharmaceuticals in sentinel lymph-node detection—An overview. Eur J Nucl Med. 1999;26:S36–42.

42. Noguchi M. Sentinel lymph node biopsy and breast cancer. Br J Surg. 2002;89:21–34.

43. Trifirò G, Viale G, Gentilini O, et al. Sentinel node detection in pre-operative axillary staging. Eur J Nucl Med Mol Imaging. 2004;31:S46–55.

44. Leidenius MH, Leppänen EA, Krogerus LA, et al. The impact of radiopharmaceutical particle size on the visualization and identification of sentinel nodes in breast cancer. Nucl Med Commun. 2004;25:233–8.

45. Nieweg OE, Jansen L, Valdés Olmos RA, et al. Lymphatic mapping and sentinel lymph node biopsy in breast cancer. Eur J Nucl Med. 1999;26:S11–6.

46. Chinol M, Paganelli G. Current status of commercial colloidal preparations for sentinel lymph node detection. Eur J Nucl Med. 1999;26:560.

47. Vera DR, Wallace AM, Hoh CK, et al. A synthetic macromolecule for sentinel node detection: ^{99m}Tc-DTPA-mannosyl-dextran. J Nucl Med. 2001;42:951–9.

48. Heuveling DA, Visser GW, Baclayon M, et al. ^{89}Zr-nanocolloidal albumin-based PET/CT lymphoscintigraphy for sentinel node detection in head and neck cancer: preclinical results. J Nucl Med. 2011;52:1580–4.

49. Hou G, Hou B, Jiang Y, et al. ^{68}Ga-NOTA-Evans blue TOF PET/MR lymphoscintigraphy evaluation of the severity of lower limb lymphedema. Clin Nucl Med. 2019;44:439–45.

50. Niu G, Lang L, Kiesewetter DO, et al. In vivo labeling of serum albumin for PET. J Nucl Med. 2014;55:1150–6.

51. Bourgeois P. Scintigraphic investigations of the lymphatic system: the influence of injected volume and quantity of labeled colloidal tracer. J Nucl Med. 2007;48:693–5.

52. Valdés-Olmos RA, Jansen L, Hoefnagel CA, et al. Evaluation of mammary lymphoscintigraphy by a single intratumoral injection for sentinel node identification. J Nucl Med. 2000;41:1500–6.

53. Werner JA, Dünne AA, Ramaswamy A, et al. Number and location of radiolabeled, intraoperatively identified sentinel nodes in 48 head and neck cancer patients with clinically staged N0 and N1 neck. Eur Arch Otorhinolaryngol. 2002;259:91–6.

54. Ikomi F, Hunt J, Hanna G, et al. Interstitial fluid, plasma protein, colloid, and leukocyte uptake into initial lymphatics. J Appl Physiol (1985). 1996;81:2060–7.

55. O'Morchoe CC, Jones WR, Jarosz HM, et al. Temperature dependence of protein transport across lymphatic endothelium in vitro. J Cell Biol. 1984;98:629–40.

56. Lund T, Wiig H, Reed RK, et al. A "new" mechanism for oedema generation: strongly negative interstitial fluid pressure causes rapid fluid flow into thermally injured skin. Acta Physiol Scand. 1987;129:433–5.

57. Engeset A, Sokolowski J, Olszewski WL. Variation in output of leukocytes and erythrocytes in human peripheral lymph during rest and activity. Lymphology. 1977;10:198–203.

58. Olszewski W, Engeset A, Jaeger PM, et al. Flow and composition of leg lymph in normal men during venous stasis, muscular activity and local hyperthermia. Acta Physiol Scand. 1977;99:149–55.

59. Thorek DL, Abou DS, Beattie BJ, et al. Positron lymphography: multimodal, high-resolution, dynamic mapping and resection of lymph nodes after intradermal injection of ^{18}F-FDG. J Nucl Med. 2012;53:1438–45.

60. Long X, Zhang J, Zhang D, et al. Microsurgery guided by sequential preoperative lymphography using ^{68}Ga-NEB PET and MRI in patients with lower-limb lymphedema. Eur J Nucl Med Mol Imaging. 2017;44:1501–10.

61. Gibson JG, Evans WA. Clinical studies of the blood volume I. Clinical application of a method employing the azo dye "Evans Blue" and the spectrophotometer. J Clin Invest. 1937;16:301–16.

62. Torabi M, Aquino SL, Harisinghani MG. Current concepts in lymph node imaging. J Nucl Med. 2004;45:1509–18.

63. Zhang J, Lang L, Zhu Z, et al. Clinical translation of an albumin-binding PET radiotracer ^{68}Ga-NEB. J Nucl Med. 2015;56:1609–14.

64. Lusic H, Grinstaff MW. X-ray-computed tomography contrast agents. Chem Rev. 2013;113:1641–66.

65. Bae KT, Heiken JP, Brink JA. Aortic and hepatic contrast medium enhancement at CT. Part I. Prediction with a computer model. Radiology. 1998;207:647–55.

66. Bae KT. Intravenous contrast medium administration and scan timing at CT: considerations and approaches. Radiology. 2010;256:32–61.

67. Riella MC. Nephrologists Sans Frontières: a Kidney Foundation—advancing research and helping patients meet their needs. Kidney Int. 2006;69:1285–7.

68. Hizoh I, Haller C. Radiocontrast-induced renal tubular cell apoptosis: hypertonic versus oxidative stress. Invest Radiol. 2002;37:428–34.

69. Morcos SK, Thomsen HS, Webb JA. Contrast-media-induced nephrotoxicity: a consensus report. Contrast Media Safety Committee, European Society of Urogenital Radiology (ESUR). Eur Radiol. 1999;9:1602–13.

70. Jost G, Pietsch H, Lengsfeld P, et al. The impact of the viscosity and osmolality of iodine contrast agents on renal elimination. Invest Radiol. 2010;45:255–61.

71. Jost G, Pietsch H, Sommer J, et al. Retention of iodine and expression of biomarkers for renal damage in the kidney after application of iodinated contrast media in rats. Invest Radiol. 2009;44:114–23.

72. Pietsch H, Kies Sling F. Small animal imaging basics and practical guide. New York: Springer; 2011.

73. Mattrey RF, Aguirre DA. Advances in contrast media research. Acad Radiol. 2003;10:1450–60.

74. Hallouard F, Anton N, Choquet P, et al. Iodinated blood pool contrast media for preclinical X-ray imaging applications—A review. Biomaterials. 2010;31:6249–68.

75. Idé JM, Lancelot E, Pines E, et al. Prophylaxis of iodinated contrast media-induced nephropathy: a pharmacological point of view. Invest Radiol. 2004;39:155–70.

76. Chung YE, Hyung WJ, Kweon S, et al. Feasibility of interstitial CT lymphography using optimized iodized oil emulsion in rats. Invest Radiol. 2010;45:142–8.

77. Wisner ER, Katzberg RW, Griffey SM, et al. Characterization of normal and cancerous lymph nodes on indirect computed tomography lymphographic studies after interstitial injection of iodinated nanoparticles. Acad Radiol. 1996;3:S257–60.

78. Gries H. Extracellular MRI contrast agents based on gadolinium. In: Krause W, editor. Contrast agents I: magnetic resonance imaging. Berlin: Springer; 2002. p. 1–24.

79. Brasch RC, Weinmann HJ, Wesbey GE. Contrast-enhanced NMR imaging: animal studies using gadolinium-DTPA complex. AJR Am J Roentgenol. 1984;142:625–30.

80. Strich G, Hagan PL, Gerber KH, et al. Tissue distribution and magnetic resonance spin lattice relaxation effects of gadolinium-DTPA. Radiology. 1985;154:723–6.

81. Schmiedl U, Ogan M, Paajanen H, et al. Albumin labeled with Gd-DTPA as an intravascular, blood pool-enhancing agent for MR imaging: biodistribution and imaging studies. Radiology. 1987;162:205–10.

82. Pathak AP, Artemov D, Neeman M, et al. Lymph node metastasis in breast cancer xenografts is associated with increased regions of extravascular drain, lymphatic vessel area, and invasive phenotype. Cancer Res. 2006;66:5151–8.

83. Li C, Meng S, Yang X, et al. Sentinel lymph node detection using magnetic resonance lymphography with conventional gadolinium contrast agent in breast cancer: a preliminary clinical study. BMC Cancer. 2015;15:213.

84. Shiozawa M, Kobayashi S, Sato Y, et al. Magnetic resonance lymphography of sentinel lymph nodes in patients with breast cancer using superparamagnetic iron oxide: a feasibility study. Breast Cancer. 2014;21:394–401.

85. Tangoku A, Yamamoto S, Suga K, et al. Sentinel lymph node biopsy using computed tomography-lymphography in patients with breast cancer. Surgery. 2004;135:258–65.

86. Kobayashi H, Kawamoto S, Choyke PL, et al. Comparison of dendrimer-based macromolecular contrast agents for dynamic micro-magnetic resonance lymphangiography. Magn Reson Med. 2003;50:758–66.

87. Mounzer R, Shkarin P, Papademetris X, et al. Dynamic imaging of lymphatic vessels and lymph nodes using a bimodal nanoparticulate contrast agent. Lymphat Res Biol. 2007;5:151–8.

88. Cheng Z, Al Zaki A, Jones IW, et al. Stabilized porous liposomes with encapsulated Gd-labeled dextran as a highly efficient MRI contrast agent. Chem Commun (Camb). 2014;50:2502–4.

89. Ishiguchi T, Takahashi S. Safety of gadoterate meglumine (Gd-DOTA) as a contrast agent for magnetic resonance imaging. Drugs R&D. 2010;10:133–45.

90. Shimada M, Yoshikawa K, Suganuma T, et al. Interstitial magnetic resonance lymphography: comparative animal study of gadofluorine 8 and gadolinium diethylenetriamine-pentaacetic acid. J Comput Assist Tomogr. 2003;27:641–6.

91. Normann PT, Hals PA. In vivo stability and excretion of gadodiamide (GdDTPA-BMA), a hydrophilic gadolinium complex used as a contrast enhancing agent for magnetic resonance imaging. Eur J Drug Metab Pharmacokinet. 1995;20:307–13.

92. Cho SB, Lee AL, Chang HW, et al. Prospective multicenter study of the safety of gadoteridol in 6163 patients. J Magn Reson Imaging. 2020;51:861–8.

93. Baker JF, Kratz LC, Stevens GR, et al. Pharmacokinetics and safety of the MRI contrast agent gadoversetamide injection (OptiMARK) in healthy pediatric subjects. Invest Radiol. 2004;39:334–9.

94. Kobayashi H, Kawamoto S, Sakai Y, et al. Lymphatic drainage imaging of breast cancer in mice by micro-magnetic resonance lymphangiography using a nano-size paramagnetic contrast agent. J Natl Cancer Inst. 2004;96:703–8.

95. Kobayashi H, Kawamoto S, Brechbiel MW, et al. Detection of lymph node involvement in hematologic malignancies using micromagnetic resonance lymphangiography with a gadolinium-labeled dendrimer nanoparticle. Neoplasia. 2005;7:984–91.

96. Talanov VS, Regino CA, Kobayashi H, et al. Dendrimer-based nanoprobe for dual modality magnetic resonance and fluorescence imaging. Nano Lett. 2006;6:1459–63.

97. Ma X, Wang S, Hu L, et al. Imaging characteristics of USPIO nanoparticles (<5 nm) as MR contrast agent. Contrast Media Mol Imaging. 2019;2019:3687537.

98. Xiao YD, Paudel R, Liu J, et al. MRI contrast agents: classification and application (review). Int J Mol Med. 2016;38:1319–26.

99. Wang YX, Hussain SM, Krestin GP. Superparamagnetic iron oxide contrast agents: physicochemical characteristics and applications in MR imaging. Eur Radiol. 2001;11:2319–31.

100. Weissleder R. Molecular imaging: principles and practice. PMPH-USA: Raleigh; 2010.

101. Elias A, Tsourkas A. Imaging circulating cells and lymphoid tissues with iron oxide nanoparticles. Hematology Am Soc Hematol Educ Program. 2009:720–6.

102. Wei H, Bruns OT, Kaul MG, et al. Exceedingly small iron oxide nanoparticles as positive MRI contrast agents. Proc Natl Acad Sci U S A. 2017;114:2325–30.

103. McCarthy JR, Weissleder R. Multifunctional magnetic nanoparticles for targeted imaging and therapy. Adv Drug Deliv Rev. 2008;60:1241–51.

104. Ittrich H, Peldschus K, Raabe N, et al. Superparamagnetic iron oxide nanoparticles in biomedicine: applications and developments in diagnostics and therapy. Rofo. 2013;185:1149–66.

105. Weissleder R, Stark DD, Engelstad BL, et al. Superparamagnetic iron oxide: pharmacokinetics and toxicity. AJR Am J Roentgenol. 1989;152:167–73.

106. Bellin MF, Lebleu L, Meric JB. Evaluation of retroperitoneal and pelvic lymph node metastases with MRI and MR lymphangiography. Abdom Imaging. 2003;28:155–63.

107. Anzai Y, McLachlan S, Morris M, et al. Dextran-coated superparamagnetic iron oxide, an MR contrast agent for assessing lymph nodes in the head and neck. AJNR Am J Neuroradiol. 1994;15:87–94.

108. Hudgins PA, Anzai Y, Morris MR, et al. Ferumoxtran-10, a superparamagnetic iron oxide as a magnetic resonance enhancement agent for imaging lymph nodes: a phase 2 dose study. AJNR Am J Neuroradiol. 2002;23:649–56.

109. Dewitte H, Vanderperren K, Haers H, et al. Theranostic mRNA-loaded microbubbles in the lymphatics of dogs: implications for drug delivery. Theranostics. 2015;5:97–109.

110. Yoon YI, Kwon YS, Cho HS, et al. Ultrasound-mediated gene and drug delivery using a microbubble-liposome particle system. Theranostics. 2014;4:1133–44.

111. Jian J, Liu C, Gong Y, et al. India ink incorporated multifunctional phase-transition nanodroplets for photoacoustic/ultrasound dual-modality imaging and photoacoustic effect based tumor therapy. Theranostics. 2014;4:1026–38.

112. Fan CH, Lin WH, Ting CY, et al. Contrast-enhanced ultrasound imaging for the detection of focused ultrasound-induced blood-brain barrier opening. Theranostics. 2014;4:1014–25.

113. Liu HL, Fan CH, Ting CY, et al. Combining microbubbles and ultrasound for drug delivery to brain tumors: current progress and overview. Theranostics. 2014;4:432–44.

114. Vlaisavljevich E, Durmaz YY, Maxwell A, et al. Nanodroplet-mediated histotripsy for image-guided targeted ultrasound cell ablation. Theranostics. 2013;3:851–64.

115. Sirsi SR, Fung C, Garg S, et al. Lung surfactant microbubbles increase lipophilic drug payload for ultrasound-targeted delivery. Theranostics. 2013;3:409–19.

116. Streeter JE, Dayton PA. An in vivo evaluation of the effect of repeated administration and clearance of targeted contrast agents on molecular imaging signal enhancement. Theranostics. 2013;3:93–8.

117. Greis C. Ultrasound contrast agents as markers of vascularity and microcirculation. Clin Hemorheol Microcirc. 2009;43:1–9.

118. Stride E. Physical principles of microbubbles for ultrasound imaging and therapy. Cerebrovasc Dis. 2009;27:1–13.

119. Klibanov AL, Rasche PT, Hughes MS, et al. Detection of individual microbubbles of ultrasound contrast agents: imaging of free-floating and targeted bubbles. Invest Radiol. 2004;39:187–95.

120. Unnikrishnan S, Klibanov AL. Microbubbles as ultrasound contrast agents for molecular imaging: preparation and application. AJR Am J Roentgenol. 2012;199:292–9.

121. Bzyl J, Lederle W, Rix A, et al. Molecular and functional ultrasound imaging in differently aggressive breast cancer xenografts using two novel ultrasound contrast agents (BR55 and BR38). Eur Radiol. 2011;21:1988–95.

122. Walday P, Tolleshaug H, Gjøen T, et al. Biodistributions of air-filled albumin microspheres in rats and pigs. Biochem J. 1994;299:437–43.

123. Perkins AC, Frier M, Hindle AJ, et al. Human biodistribution of an ultrasound contrast agent (Quantison) by radiolabelling and gamma scintigraphy. Br J Radiol. 1997;70:603–11.

124. Jakobsen JA, Oyen R, Thomsen HS, et al. Members of Contrast Media Safety Committee of European Society of Urogenital Radiology (ESUR). Safety of ultrasound contrast agents. Eur Radiol. 2005;15:941–5.

125. Piscaglia F, Bolondi L. Italian Society for Ultrasound in Medicine and Biology (SIUMB) Study Group on Ultrasound Contrast Agents. The safety of Sonovue in abdominal applications: retrospective analysis of 23188 investigations. Ultrasound Med Biol. 2006;32:1369–75.

126. Main ML, Ryan AC, Davis TE, et al. Acute mortality in hospitalized patients undergoing echocardiography with and without an ultrasound contrast agent (multicenter registry results in 4,300,966 consecutive patients). Am J Cardiol. 2008;102:1742–6.

127. Lindner JR, Coggins MP, Kaul S, et al. Microbubble persistence in the microcirculation during ischemia/reperfusion and inflammation is caused by integrin- and complement-mediated adherence to activated leukocytes. Circulation. 2000;101:668–75.

128. Lurie DM, Seguin B, Schneider PD, et al. Contrast-assisted ultrasound for sentinel lymph node detection in spontaneously arising canine head and neck tumors. Invest Radiol. 2006;41:415–21.

129. Sever A, Jones S, Cox K, et al. Preoperative localization of sentinel lymph nodes using intradermal microbubbles and contrast-enhanced ultrasonography in patients with breast cancer. Br J Surg. 2009;96:1295–9.

130. Goldberg BB, Merton DA, Liu JB, et al. Sentinel lymph nodes in a swine model with melanoma: contrast-enhanced lymphatic US. Radiology. 2004;230:727–34.

131. Ravizzini G, Turkbey B, Barrett T, et al. Nanoparticles in sentinel lymph node mapping. Wiley Interdiscip Rev Nanomed Nanobiotechnol. 2009;1:610–23.

132. Wang LV, Hu S. Photoacoustic tomography: in vivo imaging from organelles to organs. Science. 2012;335:1458–62.

133. Mallidi S, Watanabe K, Timerman D, et al. Prediction of tumor recurrence and therapy monitoring using ultrasound-guided photoacoustic imaging. Theranostics. 2015;5:289–301.

134. Zhang R, Pan D, Cai X, et al. alpha$_v$beta$_3$-targeted copper nanoparticles incorporating an Sn 2 lipase-labile fumagillin prodrug for photoacoustic neovascular imaging and treatment. Theranostics. 2015;5:124–33.

135. Wilson KE, Bachawal SV, Tian L, et al. Multiparametric spectroscopic photoacoustic imaging of breast cancer development in a transgenic mouse model. Theranostics. 2014;4:1062–71.

136. Song KH, Stein EW, Margenthaler JA, et al. Noninvasive photoacoustic identification of sentinel lymph nodes containing methylene blue in vivo in a rat model. J Biomed Opt. 2008;13:054033.

137. De la Zerda A, Zavaleta C, Keren S, et al. Carbon nanotubes as photoacoustic molecular imaging agents in living mice. Nat Nanotechnol. 2008;3:557–62.

138. Kim JW, Galanzha EI, Shashkov EV, et al. Golden carbon nanotubes as multimodal photoacoustic and photothermal high-contrast molecular agents. Nat Nanotechnol. 2009;4:688–94.

139. Pan D, Pramanik M, Senpan A, et al. Near infrared photoacoustic detection of sentinel lymph nodes with gold nanobeacons. Biomaterials. 2010;31:4088–93.

140. Carrington C. Optical imaging sheds light on cancer's signature—regional blood flow and tissue oxygenation measures may permit earlier breast cancer detection. Diagnost Imag. www.diagnosticimaging.com. Accessed June 2004.

141. Berlier JE, Rothe A, Buller G, et al. Quantitative comparison of long-wavelength Alexa Fluor dyes to Cy dyes: fluorescence of the dyes and their bioconjugates. J Histochem Cytochem. 2003;51:1699–712.

142. Fox IJ, Brooker LG, Heseltine DW, et al. A tricarbocyanine dye for continuous recording of dilution curves in whole blood independent of variations in blood oxygen saturation. Proc Staff Meet Mayo Clin. 1957;32:478–84.

143. Alander JT, Kaartinen I, Laakso A, et al. A review of indocyanine green fluorescent imaging in surgery. Int J Biomed Imaging. 2012;2012:940585.

144. Landsman ML, Kwant G, Mook GA, et al. Light-absorbing properties, stability, and spectral stabilization of indocyanine green. J Appl Physiol. 1976;40:575–83.

145. Desmettre T, Devoisselle JM, Mordon S. Fluorescence properties and metabolic features of indocyanine green (ICG) as related to angiography. Surv Ophthalmol. 2000;45:15–27.

146. Engel E, Schraml R, Maisch T, et al. Light-induced decomposition of indocyanine green. Invest Ophthalmol Vis Sci. 2008;49:1777–83.

147. Rosenthal SM, White EC. Clinical application of the bromsulphalein test for hepatic function. J Am Med Assoc. 1925;84:1112–4.

148. Benya R, Quintana J, Brundage B. Adverse reactions to indocyanine green: a case report and a review of the literature. Catheter Cardiovasc Diagn. 1989;17:231–3.

149. Jung SY, Kim SK, Kim SW, et al. Comparison of sentinel lymph node biopsy guided by the multimodal method of indocyanine green fluorescence, radioisotope, and blue dye versus the radioisotope method in breast cancer: a randomized controlled trial. Ann Surg Oncol. 2014;21:1254–9.

150. Martínez Bonilla CA, Kouznetsov VV. "Green" quantum dots: basics, green synthesis, and nanotechnological applications. Green Nanotechnol. 2016:173–92. https://doi.org/10.5772/62327.

151. Chan WC, Maxwell DJ, Gao X, et al. Luminescent quantum dots for multiplexed biological detection and imaging. Curr Opin Biotechnol. 2002;13:40–6.

152. Alivisatos AP, Gu W, Larabell C. Quantum dots as cellular probes. Annu Rev Biomed Eng. 2005;7:55–76.

153. Hama Y, Koyama Y, Urano Y, et al. Simultaneous two-color spectral fluorescence lymphangiography with near infrared quantum dots to map two lymphatic flows from the breast and the upper extremity. Breast Cancer Res Treat. 2007;103:23–8.

154. Kim S, Lim YT, Soltesz EG, et al. Near-infrared fluorescent type II quantum dots for sentinel lymph node mapping. Nat Biotechnol. 2004;22:93–7.

155. Ow H, Larson DR, Srivastava M, et al. Bright and stable core-shell fluorescent silica nanoparticles. Nano Lett. 2005;5:113–7.

156. Padera TP, Stoll BR, So PT, et al. Conventional and high-speed intravital multiphoton laser scanning microscopy of microvasculature, lymphatics, and leukocyte-endothelial interactions. Mol Imaging. 2002;1:9–15.

157. Leu AJ, Gretener SB, Enderlin S, et al. Lymphatic microangiopathy of the skin in systemic sclerosis. Rheumatology (Oxford). 1999;38:221–7.

158. Seibold U, Wängler B, Schirrmacher R, et al. Bimodal imaging probes for combined PET and OI: recent developments and future directions for hybrid agent development. Biomed Res Int. 2014;2014:153741.

159. Culver J, Akers W, Achilefu S. Multimodality molecular imaging with combined optical and SPECT/PET modalities. J Nucl Med. 2008;49:169–72.

160. Tsopelas C, Bevington E, Kollias J, et al. ^{99m}Tc-Evans blue dye for mapping contiguous lymph node sequences and discriminating the sentinel lymph node in an ovine model. Ann Surg Oncol. 2006;13:692–700.

161. Brouwer OR, Buckle T, Vermeeren L, et al. Comparing the hybrid fluorescent-radioactive tracer indocyanine green-^{99m}Tc-nanocolloid with ^{99m}Tc-nanocolloid for sentinel node identification: a validation study using lymphoscintigraphy and SPECT/CT. J Nucl Med. 2012;53:1034–40.

162. Koyama Y, Talanov VS, Bernardo M, et al. A dendrimer-based nanosized contrast agent dual-labeled for magnetic resonance and optical fluorescence imaging to localize the sentinel lymph node in mice. J Magn Reson Imaging. 2007;25:866–71.

163. Choi JS, Park JC, Nah H, et al. A hybrid nanoparticle probe for dual-modality positron emission tomography and magnetic resonance imaging. Angew Chem Int Ed Engl. 2008;47:6259–62.

164. Yang BY, Moon SH, Seelam SR, et al. Development of a multimodal imaging probe by encapsulating iron oxide nanoparticles with functionalized amphiphiles for lymph node imaging. Nanomedicine (Lond). 2015;10:1899–910.

165. Torres Martin de Rosales R, Tavaré R, Paul RL, et al. Synthesis of 64Cu(II)-bis(dithiocarbamatebisphosphonate) and its conjugation with superparamagnetic iron oxide nanoparticles: in vivo evaluation as dual-modality PET-MRI agent. Angew Chem Int Ed Engl. 2011;50:5509–13.

166. Madru R, Kjellman P, Olsson F, et al. ^{99m}Tc-labeled superparamagnetic iron oxide nanoparticles for multimodality SPECT/MRI of sentinel lymph nodes. J Nucl Med. 2012;53:459–63.

167. Chakravarty R, Valdovinos HF, Chen F, et al. Intrinsically germanium-69-labeled iron oxide nanoparticles: synthesis and in-vivo dual-modality PET/MR imaging. Adv Mater. 2014;26:5119–23.

168. Thorek DL, Ulmert D, Diop NF, et al. Non-invasive mapping of deep-tissue lymph nodes in live animals using a multimodal PET/MRI nanoparticle. Nat Commun. 2014;5:3097.

169. Park JC, Yu MK, An GI, et al. Facile preparation of a hybrid nanoprobe for triple-modality optical/PET/MR imaging. Small. 2010;6:2863–8.

170. Madru R, Tran TA, Axelsson J, et al. ^{68}Ga-labeled superparamagnetic iron oxide nanoparticles (SPIONs) for multi-modality PET/MR/Cherenkov luminescence imaging of sentinel lymph nodes. Am J Nucl Med Mol Imaging. 2013;4:60–9.

171. Kim JS, Kim YH, Kim JH, et al. Development and in vivo imaging of a PET/MRI nanoprobe with enhanced NIR fluorescence by dye encapsulation. Nanomedicine (Lond). 2012;7:219–29.

172. Cui X, Mathe D, Kovács N, et al. Synthesis, characterization, and application of Core-Shell Co0.16Fe2.84O4@NaYF4(Yb, Er) and Fe3O4@NaYF4(Yb, Tm) nanoparticle as Trimodal (MRI, PET/SPECT, and optical) imaging agents. Bioconjug Chem. 2016;27:319–28.

173. Huang X, Zhang F, Lee S, et al. Long-term multimodal imaging of tumor draining sentinel lymph nodes using mesoporous silica-based nanoprobes. Biomaterials. 2012;33:4370–8.

174. Mathelin C, Piqueras I, Guyonnet JL. Development of technologies for sentinel lymph node biopsy in case of breast cancer. Gynecol Obstet Fertil. 2006;34:521–5.

175. Povoski SP, Neff RL, Mojzisik CM, et al. A comprehensive overview of radioguided surgery using gamma detection probe technology. World J Surg Oncol. 2009;7:11.

176. Woolfenden JM, Barber HB. Radiation detector probes for tumor localization using tumor-seeking radioactive tracers. AJR Am J Roentgenol. 1989;153:35–9.

177. Kwo DP, Barber HB, Barrett HH, et al. Comparison of NaI(T1), CdTe, and HgI2 surgical probes: effect of scatter compensation on probe performance. Med Phys. 1991;18:382–9.

178. Tiourina T, Arends B, Huysmans D, et al. Evaluation of surgical gamma probes for radioguided sentinel node localisation. Eur J Nucl Med. 1998;25:1224–31.

179. Schneebaum S, Even-Sapir E, Cohen M, et al. Clinical applications of gamma-detection probes—radioguided surgery. Eur J Nucl Med. 1999;26:S26–35.

180. Hoffman EJ, Tornai MP, Janecek M, et al. Intraoperative probes and imaging probes. Eur J Nucl Med. 1999;26:913–35.

181. Zanzonico P, Heller S. The intraoperative gamma probe: basic principles and choices available. Semin Nucl Med. 2000;30:33–48.

182. Mariani G, Vaiano A, Nibale O, et al. Is the "ideal" gamma-probe for intraoperative radioguided surgery conceivable? J Nucl Med. 2005;46:388–90.

183. Moffat FL. Targeting gold at the end of the rainbow: surgical gamma probes in the 21st century. J Surg Oncol. 2007;96:286–9.

184. Ricard M. Intraoperative detection of radiolabeled compounds using a hand held gamma probe. Nucl Instrum Method Phys Res A. 2001;458:26–33.

185. Guided intraoperative scintigraphic tumour targeting (GOSTT)—Implementing advanced hybrid molecular imaging and non-imaging probes for advanced cancer management. Vienna: IAEA Human Health Series; 2014.

186. Herrmann K, Nieweg OE, Povoski SP. Radioguided surgery. In: Current applications and innovative directions in clinical practice. Berlin: Springer; 2016.

187. Povoski SP, Chapman GJ, Murrey DA, et al. Intraoperative detection of ^{18}F-FDG-avid tissue sites using the increased probe counting efficiency of the K-alpha probe design and variance-based statistical analysis with the three-sigma criteria. BMC Cancer. 2013;13:98.

188. Povoski SP, Hall NC, Murrey DA, et al. Feasibility of a multimodal ^{18}F-FDG-directed lymph node surgical excisional biopsy approach for appropriate diagnostic tissue sampling in patients with suspected lymphoma. BMC Cancer. 2015;15:378.

189. Sarikaya I, Sarikaya A, Reba RC. Gamma probes and their use in tumor detection in colorectal cancer. Int Semin Surg Oncol. 2008;5:25.

190. RMD. Instruments Corp. https://www.surgeonschoice.net.au/Navigator_GPS_Manual.pdf. Accessed 10 Dec 2019.
191. Gamma Finder® II, W.O.M. World of Medicine AG. http://www.mesamedical.co.kr/new/DATA/mesa_hBUSINESS/7_mesa_hBUSINESS_FN04.pdf. Accessed 10 Dec 2019.
192. Bluetooth® Gamma Detection Probe, Neoprobe Corporation. http://www.hospiline.com.br/mammotome/documents/Products/Neoprobe/Model1100and1101OpsManualEngli.pdf. Accessed 10 Dec 2019.
193. Sentinella s-102. https://oncovision.com/sentinella/. Accessed 10 Dec 2019.
194. Anzai eZ-scope. http://www.nuclemed.be; https://www.access-data.fda.gov/cdrh_docs/pdf9/K092471.pdf. Accessed 10 Dec 2019.
195. LumaGEM. http://www.cmr-naviscan.com/lumagem/. Accessed 10 Dec 2019.
196. Heckathorne E, Tiefer L, Daghighian F, et al. Evaluation of arrays of silicon photomultipliers for beta imaging. Nuclear Science Symposium Conference Record. 2008:1626–31.
197. Singh B, Stack BC, Thacker S, et al. A hand-held beta imaging probe for FDG. Ann Nucl Med. 2013;27:203–8.
198. DSouza AV, Lin H, Henderson ER, et al. Review of fluorescence guided surgery systems: identification of key performance capabilities beyond indocyanine green imaging. J Biomed Opt. 2016;21:80901.
199. Kim DW, Jeong B, Shin IH, et al. Sentinel node navigation surgery using near-infrared indocyanine green fluorescence in early gastric cancer. Surg Endosc. 2019;33:1235–43.
200. Kong SH, Bae SW, Suh YS, et al. Near-infrared fluorescence lymph node navigation using indocyanine green for gastric cancer surgery. J Minim Invasive Surg. 2018;21:95–105.
201. Duprée A, Rieß H, Detter C, et al. Utilization of indocyanine green fluorescent imaging (ICG-FI) for the assessment of micro-perfusion in vascular medicine. Innov Surg Sci. 2018;3:193–201.